

Consistent dust and gas models for protoplanetary disks

II. Chemical networks and rates

I. Kamp¹, W.-F. Thi², P. Woitke³, C. Rab⁴, S. Bouma¹, and F. Ménard⁵

¹ Kapteyn Astronomical Institute, University of Groningen, Postbus 800, 9700 AV Groningen, The Netherlands

² Max Planck Institute for Extraterrestrial Physics, Giessenbachstrasse, 85741 Garching, Germany

³ SUPA, School of Physics & Astronomy, University of St. Andrews, North Haugh, St. Andrews, KY16 9SS, UK

⁴ University of Vienna, Department for Astrophysics, Türkenschanzstr.17, 1180 Vienna, Austria

⁵ University of Grenoble Alpes, CNRS, IPAG, F-38000 Grenoble, France

Received ; accepted

ABSTRACT

Aims. We define a small and large chemical network which can be used for the quantitative simultaneous analysis of molecular emission from the near-IR to the submm. We revise reactions of excited molecular hydrogen, which are not included in UMIST, to provide a homogeneous database for future applications.

Methods. We use the thermo-chemical disk modeling code ProDiMo and a standard T Tauri disk model to evaluate the impact of various chemical networks, reaction rate databases and sets of adsorption energies on a large sample of chemical species and emerging line fluxes from the near-IR to the submm wavelength range.

Results. We find large differences in the masses and radial distribution of ice reservoirs when considering freeze-out on bare or polar ice coated grains. Most strongly the ammonia ice mass and the location of the snow line (water) change. As a consequence molecules associated to the ice lines such as N_2H^+ change their emitting region; none of the line fluxes in the sample considered here changes by more than 25% except CO isotopologues, CN and N_2H^+ lines. The three-body reaction $N+H_2+M$ plays a key role in the formation of water in the outer disk. Besides that, differences between the UMIST 2006 and 2012 database change line fluxes in the sample considered here by less than a factor 2 (a subset of low excitation CO and fine structure lines stays even within 25%); exceptions are OH, CN, HCN, HCO^+ and N_2H^+ lines. However, different networks such as OSU and KIDA 2011 lead to pronounced differences in the chemistry inside 100 au and thus affect emission lines from high excitation CO, OH and CN lines. H_2 is easily excited at the disk surface and state-to-state reactions enhance the abundance of CH^+ and to a lesser extent HCO^+ . For sub-mm lines of HCN, N_2H^+ and HCO^+ , a more complex larger network is recommended.

Conclusions. More work is required to consolidate data on key reactions leading to the formation of water, molecular ions such as HCO^+ and N_2H^+ as well as the nitrogen chemistry. This affects many of the key lines used in the interpretation of disk observations. Differential analysis of various disk models using the same chemical input data will be more robust than the interpretation of absolute fluxes.

Key words. astrochemistry; molecular data; protoplanetary disks; Methods: numerical

1. Introduction

Observations often detect a multitude of simple molecules which have bright emission lines in protoplanetary disks such as CO, HCO^+ , HCN, CN, N_2H^+ , H_2CO , CH^+ (e.g. Thi et al. 2004; Dutrey et al. 2007; Öberg et al. 2010; Thi et al. 2011a; Qi et al. 2013a). Even though studying differences in the molecular content of disks is interesting in its own right, molecules are frequently used as tracers of disk properties, such as outer gas radius (e.g. Panić & Hogerheijde 2009), the position of the CO ice line (e.g. Qi et al. 2013b), the ionization degree (e.g. Qi et al. 2003), the irradiation by X-rays (e.g. Aikawa & Herbst 2001) and the deuterium fractionation (e.g. Ceccarelli et al. 2005).

Due to the importance of molecular lines for protoplanetary disk research, several studies have focussed on the size of chemical networks and the uncertainties in chemical rates. Semenov et al. (2004) find that the midplane and the ionized surface layer can be described using very small networks, while the intermediate layer, where most of the ion-molecule chemistry happens, requires large networks with of the order of 100 species. Vasyunin et al. (2004) varied the rate constants within

the uncertainties using a Monte Carlo approach and conditions representative of diffuse and dark clouds. In dark clouds, they find abundance changes of less than 0.5 dex for simple species such as N_2H^+ , HCO^+ , while HCN can change up to 1 dex. Interestingly, CO is among the most robust species. Vasyunin et al. (2008) expanded this study to protoplanetary disk conditions. Again, CO is the most robust species while HCN, N_2H^+ , and HCO^+ column densities can typically vary by a factor 2.5-3. Local changes can, however, be larger than this.

Thermo-chemical disk models often use a single network throughout the entire disk. When comparing such models to a set of observational data including molecular emission lines, we often rely in a first step on simple molecules such as CO and HCN. For those molecules, the chemistry is simple, resulting in robust model predictions. The chemical network used in this step should be small and fast to solve in order to allow the computation of larger model grids or the use of evolutionary search strategies to derive basic properties of the disk such as the dust mass, the mass of CO gas, radial extent of the disk, and the amount of flaring. In a second step, based on the previously found disk model, species with a more complex chemistry can

be studied using larger chemical networks. It is important however to note that the chemical network is only one aspect in the interpretation of line observations. The other one, which is not addressed in this work, is the calculation of the excitation of the molecule which can be limited by the availability of molecular data (mainly collision cross sections), the complexity of IR and UV pumping or resonance scattering for optically thick lines (e.g. Cernicharo et al. 2009; Bethell & Bergin 2011; Kamp et al. 2013; Thi et al. 2013).

We develop in this paper simple rules for the construction of chemical networks that avoid artificial sinks and ensure links between various sub-networks such as the carbon, oxygen and nitrogen chemistry. We use a standard T Tauri disk model from Woitke et al. (2016) to study the impact of the size of the network, different chemical databases and ice adsorption scenarios on the species mass and emission from a representative sample of atomic and molecular lines (Sect. 2). Woitke et al. (2016) show that time-dependent chemistry has little effect on the resulting line fluxes at ages beyond 0.5 Myr. Hence, we focus here entirely on stationary chemistry. In Section 3, we discuss how changes in the UMIST database and the use of other databases affect the disk chemistry and line emission (Sect. 3.2, 3.3). We investigate the role of three-body reactions for water chemistry (Sect. 3.3) and how the composition of the grains (bare or polar ices) affects the various ices reservoirs and emission lines connected to them (Sect. 3.4). We study the importance of reactions with excited molecular hydrogen (Sect. 3.5) and we end with assessing which emission lines require the use of larger chemical networks (Sect. 3.6).

2. The modeling

2.1. The disk model

We choose for this study a parametrized disk structure representative of a typical T Tauri star. The full model is described in Woitke et al. (2016). Table 1 repeats only the most important stellar and disk parameters.

Table 1. Basic model parameters for the standard T Tauri disk.

Quantity	Symbol	Value
Stellar mass	M_*	$0.7 M_\odot$
Effective temperature	T_{eff}	4000 K
Stellar luminosity	L_*	$1.0 L_\odot$
FUV excess	f_{UV}	0.01
	p_{UV}	1.3
Cosmic ray ionization rate	ζ_{CR}	$1.7 \cdot 10^{-17} \text{ s}^{-1}$
Chemical heating efficiency	γ^{chem}	0.2
Disk gas mass ¹	M_{gas}	$0.033 M_\odot$
dust-to-gas mass ratio	δ	0.01
Inner disk radius	R_{in}	0.07 au
Outer disk radius ²	R_{out}	700 au
Tapered edge radius	R_{taper}	100 au
Radial column density power index	ϵ	1.0
Reference radius	R_0	100 au
Scale height at R_0	H_0	10.0 au
Disk flaring power index	β	1.15
Minimum dust particle radius	a_{min}	$0.05 \mu\text{m}$
Maximum dust particle radius	a_{max}	$3000.0 \mu\text{m}$
Dust size distribution power index	a_{pow}	3.5

Notes. (1) The disk mass is a factor 3.3 higher than in the original Woitke et al. (2016) model. (2) The outer radius is defined as the radius where the surface density column drops to $N_{(\text{H}),\text{ver}} = 10^{20} \text{ cm}^{-2}$.

Table 2. Series of disk models: the columns denote the set of adsorption energies E_{ads} , chemical network and rate database used.

model	E_{ads}	network size, mode	base rates
model 1	Aikawa	small, steady state	UMIST2012 + CL reactions
model 2	Aikawa	small, steady state	UMIST2006
model 3	Aikawa	small, steady state	OSU
model 4	Aikawa	small, steady state	KIDA2011
model 1a	Aikawa	small, steady state	UMIST2012
model 5	GH06	small, steady state	UMIST2012 + CL reactions
model 6	UMIST2012	small, steady state	UMIST2012 + CL reactions
model 7	T -dependent	small, steady state	UMIST2012 + CL reactions
model 8	UMIST2012	large, steady state	UMIST2012 + CL reactions

To calculate the two dimensional physical and chemical structure, we use the radiation thermo-chemical disk code ProDiMo (Woitke et al. 2009a; Kamp et al. 2010; Thi et al. 2011b). The disk structure is set up using a tapered edge and mildly flaring geometry ($\beta = 1.15$). It extends from 0.07 to 700 au (characteristic radius at 100 au) and contains a gas mass of $0.033 M_\odot$. The dust grain opacities are calculated using hollow spheres and a mixture of 60% silicates and 15% amorphous carbon with 25% vacuum (Min et al. 2016b) and we use the canonical dust-to-gas mass ratio of 0.01.

We use here a model series where we vary the base set of reaction rates, the set of adsorption energies, and the size of the chemical network using stationary chemistry. The reaction rate databases are UMIST2012 (McElroy et al. 2013), UMIST2006 (Woodall et al. 2007), OSU (Ohio State University chemical network from Eric Herbst) and KIDA2011 (Wakelam et al. 2012). Three sets of adsorption energies are taken from Aikawa et al. (1996a), Garrod & Herbst (2006), and UMIST2012 (McElroy et al. 2013). The adsorption energies will be discussed in more detail in Sect. 3.4. The rules for compiling the small and large chemical network are provided in the next subsection. Table 2 describes the entire model series.

Since the disk chemistry and heating/cooling balance are intimately coupled, we fixed the gas temperature structure to that of the reference model 1 (UMIST2012, adsorption energies from Aikawa et al. 1996a). This allows us to interpret changes in the chemical structure and emitted line fluxes entirely from the various chemical input data sets. The coupling of heating/cooling and chemical equations is highly non-linear, so the impact of our approximation can only be checked from additional models. We calculated a single additional model where we used the KIDA database and re-computed the gas temperature self-consistently. Our models — discussed in more detail in the next section — show that KIDA produces less water compared to UMIST in the warm surface layer stretching to a few au at gas temperatures higher than 200 K. Indeed, the additional model shows that the gas temperature in that layer increases slightly since the water cooling is diminished with respect to the UMIST reference model. However, the effects are very subtle, if the overall gas temperature distribution is considered.

2.2. The chemical network

We follow two approaches here: (1) provide a robust and fast standard that enables to deal with simple species (robust tracers) such as C, O, Ne, CO, CN, CO₂, OH, and H₂O, (2) provide a consistent standard that can be used as a starting point for further investigation of the chemistry of more complex species such as HCN, H₂C₂, HCO⁺, N₂H⁺. So far, in the literature no chemistry standard has been defined for disks in the context of multi-wavelength fitting of observational data. Instead many different species lists are used and we only start to understand the impact of the species choices and/or presence of ices and electron sinks for the abundance of specific low abundance tracers such as HCO⁺ ($\epsilon \sim 10^{-10}$) (Kamp et al. 2013, Rab et al. in preparation).

Table 3 shows the selection used for many years in the disk modeling for the Herschel open time key program GASPS (Gas Evolution in Planetary Systems, PI: B. Dent); we subsequently refer to this as the small network. The abundances of the robust tracers listed above should be calculated with sufficient accuracy and this will be tested in Sect. 3.6.

Table 4 details the selection of chemical species in the large network. We cover the most important C/N/O chemistry and a simple S and Si chemistry. Other elements (Na, Mg, Fe, Ne, Ar) are represented only by their atoms and ions. Detailed PAH charging is used, as well as a large selection of ice species. The selection of species is largely based on the chemical networks of Prasad & Huntress (1980) (C-H, C-C chemistry), van Dishoeck (1990) (C-H chemistry) Sternberg & Dalgarno (1995) (Si-chemistry, S-H chemistry, N-Chemistry, O-H chemistry), Agundez et al. (2008) (high temperature C-H, C-C chemistry), Hily-Blant et al. (2013) (N-chemistry). The size of our network is controlled by a combination of species becoming less reactive or saturated. We apply the following rules to ensure the completeness of the chemical network used:

- Negative ions/molecules have been omitted for the time being except H⁻.
- We include for all atoms/molecules the positively charged counterpart (for elements also double charged). In some cases (HeH, HNS, HSO, CH₃O), the neutral one is missing since it is not present/has no reactions in UMIST (e.g. unstable molecule or other reasons).
- C-H chemistry processes via H₂ addition reactions up to CH₅⁺, which is the maximum hydrogenation possible. CH₅⁺ can then recombine dissociatively to give the closed-shell molecule CH₄. We proceed similarly for Si-H chemistry, thus stopping at SiH₅⁺, and for O-H chemistry, thus stopping at H₃O⁺.
- We identify the neutral more stable species to be H₂, CH₂, CH₄, C₂, C₃, C₄, C₂H₂ (acetylene), C₂H₄ (ethylene), C₃H₂ (cyclopropenylidene), HCN (hydrogen cyanide), CO, CO₂, H₂CO (formaldehyde), CH₃OH (methanol), CS (carbon monosulfide), H₂CS (thioformaldehyde), NH₃ (ammonia), NO₂, HNO (nitroxyl), N₂, H₂O, SO₂, H₂S (hydrogen sulfide), OCS (carbonyl sulfide), O₂, SiH₄ (silane), SiC (silicon carbide), SiN (silicon nitride), SiO (silicon monoxide), SiS (silicon sulfide). For those molecules, we ensure that the respective positive ion and the protonated ion are included. The exception is HNO₂⁺, which is not included in UMIST (HNO₂ is included as species in UMIST, but has no reactions).
- We decided to keep the isomers CH₃O and CH₂OH to study the gas phase formation of methanol. We also keep the isomers HNC and HCN since they are both observed. However,

we only include the ion HCN⁺ and subsequent hydrogenation.

- We included several species that link the chemical networks with each other, especially for the heavier elements such as S, N, and Si. An interesting example is the radical H₂CN (amidogen). It is formed by collisions between N and C-H chains and forms a CN bond. This connects the C-H, C-C chemistry with the nitrogen chemistry.
- Neutral atoms/molecules (including radicals) except noble gases can freeze out.

2.3. Reaction rates

ProDiMo selects from the UMIST2012 database all reactions among the species defined in the chemical network above. However, in some cases, we add additional reactions and/or overwrite UMIST reactions following the procedures described in Appendix A.1-A.7. Alternatively, we also use the UMIST2006, the OSU and the KIDA 2011 databases.

2.4. Element abundances

Table 5 describes the selection of elements and their respective abundances. These are very similar to the low-metal abundances used in the literature e.g. Lee et al. (1998). All following models adopt these low metal abundances.

2.5. The line list

Table 6 describes the list of lines used to analyse how changes in disk chemistry propagate into observable line fluxes. The atomic and molecular data is collected from LAMDA (Schöier et al. 2005), NIST and CHIANTI (Dere et al. 1997). Line fluxes are calculated using level populations from statistical equilibrium and a simplified 2D escape probability approach. Detailed radiative transfer tests show that line fluxes from escape probability are typically off by less than 50% except for close to edge on disk geometries and/or lines where a significant fraction of total emission originates from the inner rim (e.g. Woitke et al. 2009b; Antonellini et al. 2015).

Details on collision cross sections and collision partners can be found in a series of papers: atoms, ions and H₂ (Woitke et al. 2009a), CH⁺ (Thi et al. 2011a), double-ionized species (Aresu et al. 2012), CO (Thi et al. 2013), H₂O (Kamp et al. 2013). The collision data for the remaining molecules is taken from the LAMDA database. The CN collision partners are He and e; the HCO⁺ collision partner is H₂; the HCN collision partners are H₂, He and e; the OH collision partners are ortho- and para-H₂.

3. Results

3.1. The base model

The physical properties of the reference model are described in detail in Woitke et al. (2016) and we summarize here a few key features relevant for the chemical studies. The model reaches total hydrogen number densities of 10¹⁴–10¹⁶ cm³ in the midplane inside 1 au. The dust temperature decreases from ~ 1500 K at the inner rim to 100 K at ~ 1 au. Gas and dust are thermally well coupled below A_v ~ 1 (towards the disk midplane). At the disk surface above A_v = 1, the gas temperature reaches values up to several 1000 K. Only in the outer disk atmosphere beyond

Table 3. Selection of elements and chemical (gas+ice) species in the small network.

12 elements	H, He, C, N, O, Ne, Na, Mg, Si, S, Ar, Fe	
(H)	H, H ⁺ , H ⁻ , H₂ , H ₂ ⁺ , H ₃ ⁺ , H ₂ ^{exc}	7
(He)	He, He ⁺	2
(C-H)	C, C ⁺ , C ⁺⁺ , CH, CH ⁺ , CH₂ , CH ₂ ⁺ , CH ₃ , CH ₃ ⁺ , CH₄ , CH ₄ ⁺ , CH ₅ ⁺ ,	12
(C-N)	CN, CN ⁺ , HCN , HCN ⁺ , HCNH ⁺	5
(C-O)	CO , CO ⁺ , HCO, HCO ⁺ , CO₂ , CO ₂ ⁺ , HCO ₂ ⁺ ,	7
(N-H)	N, N ⁺ , N ⁺⁺ , NH, NH ⁺ , NH ₂ , NH ₂ ⁺ , NH₃ , NH ₃ ⁺ , NH ₄ ⁺	9
(N-N)	N ₂ , N ₂ ⁺ , HN ₂ ⁺ ,	3
(N-O)	NO, NO ⁺ ,	2
(O-H)	O, O ⁺ , O ⁺⁺ , OH, OH ⁺ , H₂O , H ₂ O ⁺ , H ₃ O ⁺ ,	8
(O-O)	O₂ , O ₂ ⁺ ,	2
(O-S)	SO, SO ⁺ , SO₂ , SO ₂ ⁺ , HSO ₂ ⁺	5
(S-H)	S, S ⁺ , S ⁺⁺ ,	3
(Si-H)	Si, Si ⁺ , Si ⁺⁺ , SiH, SiH ⁺ , SiH ₂ ⁺ ,	6
(Si-O)	SiO , SiO ⁺ , SiOH ⁺ ,	3
(Na)	Na, Na ⁺ , Na ⁺⁺ ,	3
(Mg)	Mg, Mg ⁺ , Mg ⁺⁺ ,	3
(Fe)	Fe, Fe ⁺ , Fe ⁺⁺ ,	3
(Ne)	Ne, Ne ⁺ , Ne ⁺⁺ ,	3
(Ar)	Ar, Ar ⁺ , Ar ⁺⁺ ,	3
ice	CO#, H ₂ O#, CO ₂ #, CH ₄ #, NH ₃ #, SiO#, SO ₂ #, O ₂ #, HCN#, N ₂ #	10
species	total	100

Notes. Neutral more stable molecules are indicated in bold font and ices are indicated by a trailing #.

Table 4. Selection of elements and chemical (gas+ice) species in the large network.

13 elements	H, He, C, N, O, Ne, Na, Mg, Si, S, Ar, Fe, PAH	
(H)	H, H ⁺ , H ⁻ , H₂ , H ₂ ⁺ , H ₃ ⁺ , H ₂ ^{exc}	7
(He)	He, He ⁺ ,	2
(He-H)	HeH ⁺ ,	1
(C-H)	C, C ⁺ , C ⁺⁺ , CH, CH ⁺ , CH ₂ , CH ₂ ⁺ , CH ₃ , CH ₃ ⁺ , CH₄ , CH ₄ ⁺ , CH ₅ ⁺ ,	12
(C-C)	C₂ , C ₂ ⁺ , C ₂ H, C ₂ H ⁺ , C₂H₂ , C ₂ H ₂ ⁺ , C ₂ H ₃ , C ₂ H ₃ ⁺ , C₂H₄ , C ₂ H ₄ ⁺ , C ₂ H ₅ , C ₂ H ₅ ⁺ , C ₃ , C ₃ ⁺ , C ₃ H, C ₃ H ⁺ , C₃H₂ , C ₃ H ₂ ⁺ , C ₃ H ₃ , C ₄ , C ₄ ⁺ , C ₄ H ⁺ ,	23
(C-N)	CN, CN ⁺ , HCN , HCN ⁺ , HCNH ⁺ , HNC, H ₂ CN, OCN, OCN ⁺ ,	9
(C-O)	CO , CO ⁺ , HCO, HCO ⁺ , CO₂ , CO ₂ ⁺ , HCO ₂ ⁺ , C ₂ O, C ₂ O ⁺ , HC ₂ O ⁺ , H₂CO , H ₂ CO ⁺ , CH ₃ O, H ₃ CO ⁺ , CH ₂ OH, CH₃OH , CH ₃ OH ⁺ , CH ₃ OH ₂ ⁺ ,	18
(C-S)	CS , CS ⁺ , HCS, HCS ⁺ , H₂C₂S , H ₂ CS ⁺ , H ₃ CS ⁺ , OCS , OCS ⁺ , HOCS ⁺ ,	10
(N-H)	N, N ⁺ , N ⁺⁺ , NH, NH ⁺ , NH ₂ , NH ₂ ⁺ , NH₃ , NH ₃ ⁺ , NH ₄ ⁺ ,	10
(N-N)	N ₂ , N ₂ ⁺ , HN ₂ ⁺ ,	3
(N-O)	NO, NO ⁺ , NO₂ , NO ₂ ⁺ , HNO , HNO ⁺ , H ₂ NO ⁺ ,	7
(N-S)	NS, NS ⁺ , HNS ⁺	3
(O-H)	O, O ⁺ , O ⁺⁺ , OH, OH ⁺ , H₂O , H ₂ O ⁺ , H ₃ O ⁺ ,	8
(O-O)	O₂ , O ₂ ⁺ , O ₂ H ⁺ ,	3
(O-S)	SO, SO ⁺ , SO₂ , SO ₂ ⁺ , HSO ₂ ⁺ ,	5
(S-H)	S, S ⁺ , S ⁺⁺ , HS, HS ⁺ , H₂S , H ₂ S ⁺ , H ₃ S ⁺ ,	8
(Si-H)	Si, Si ⁺ , Si ⁺⁺ , SiH, SiH ⁺ , SiH ₂ , SiH ₂ ⁺ , SiH ₃ , SiH ₃ ⁺ , SiH₄ , SiH ₄ ⁺ , SiH ₅ ⁺ ,	12
(Si-C)	SiC , SiC ⁺ , HCSi ⁺ ,	3
(Si-N)	SiN , SiN ⁺ , HNSi ⁺ ,	3
(Si-O)	SiO , SiO ⁺ , SiOH ⁺ ,	3
(Si-S)	SiS , SiS ⁺ , HSiS ⁺ ,	3
(Na)	Na, Na ⁺ , Na ⁺⁺ ,	3
(Mg)	Mg, Mg ⁺ , Mg ⁺⁺ ,	3
(Fe)	Fe, Fe ⁺ , Fe ⁺⁺ ,	3
(Ne)	Ne, Ne ⁺ , Ne ⁺⁺ ,	3
(Ar)	Ar, Ar ⁺ , Ar ⁺⁺ ,	3
(PAH)	PAH-, PAH, PAH ⁺ , PAH ⁺⁺ , PAH ⁺⁺⁺ ,	5
ice	all neutral gas species except noble gases have ice counterparts	64
species	total	235

Notes. Neutral more stable molecules are indicated in bold font.

Table 5. Elements, their abundances on the scale $\log n_{\text{H}} = 12$ and their masses in amu.

element	$12 + \log \epsilon$	m [amu]	element	$12 + \log \epsilon$	m [amu]
H	12.00	1.0079	Na	3.36	22.990
He	10.98	4.0026	Mg	4.03	24.305
C	8.14	12.011	Si	4.24	28.086
N	7.90	14.007	S	5.27	32.066
O	8.48	15.999	Ar	6.08	39.948
Ne	7.95	20.180	Fe	3.24	55.845

100 au and below $z/r = 0.4$ (corresponding to $\sim 20^\circ$ opening angle), the gas temperature drops below that of the dust.

The abundance distribution — using the small network — for the key species CO, CO#, CO₂, CO₂#, HCO⁺, OH, H₂O#, CN, HCN, HCN#, NH₃, NH₃# is shown in Fig 1 for the reference model (model1; note that the trailing # denotes the ice form of this species). The CO surface is reasonably well described using the PDR parameter $\log \chi / \langle n_{\text{H}} \rangle$. For values larger than -3.5 , CO is efficiently photo dissociated¹ and has abundances below $\log n_{\text{CO}} / \langle n_{\text{H}} \rangle = \log \epsilon_{\text{CO}} = -8$. Here, $\langle n_{\text{H}} \rangle$ is the total hydrogen number density. The CO ice line is reasonably well described by the $T_{\text{dust}} = 20$ K line, but a rate equilibrium approach works even better (Antonellini 2016, white dashed line). The disk shows a ring of high CO₂ abundance inside 1 au. The CO₂ ice is sandwiched between the water and CO ice reservoirs. HCO⁺ only resides in a very thin layer below the C⁺/C/CO transition when the small chemical network is used.

The OH molecule constitutes the first step in the neutral-neutral chemical pathway to water formation. It is concentrated in the surface layers of the inner disk ($r < 10$ au) where gas temperatures are between 200 and 2000 K. Just below the OH reservoir, inside 0.5 au, densities are high enough to efficiently form water with an abundance of 10^{-4} . Beyond the snow line, water freezes out onto the cold dust grains. The water ice reservoir is outlined well by a rate equilibrium approach (Antonellini 2016, yellow dashed line) or using the water vapor pressure together with the local radiation field (Min et al. 2016a, white dashed line).

The disk model contains only minute amounts of CN in the disk atmosphere ($\log \epsilon_{\text{CN}} < -8$). Instead we identify two large HCN reservoirs with $\log \epsilon_{\text{HCN}} \sim -4$, a narrow ring around 0.2 au and a broader ring between 1 and 5 au. These two reservoirs sit below the $A_{\text{V}} = 1$ surface where $T_{\text{gas}} = T_{\text{dust}}$. An additional lower abundance reservoir ($\log \epsilon_{\text{HCN}} \sim -8$) can be found in the outer disk atmosphere beyond 100 au. The most stable nitrogen bearing molecule, NH₃ is only found in a very narrow ring close to the inner rim of the disk. In this particular model, NH₃ ice plays a minor role as a nitrogen reservoir.

Some of these results will depend on the details of the chosen disk model, on the set of adsorption energies used and also on the size of the chemical network. The impact of the latter two will be discussed in the subsequent sections.

Table 6. Lines used to analyse flux changes related to chemistry.

species	designation	E_{up} [K]	A_{ij} [s ⁻¹]	λ [μm]
CO	J=2-1	16.60	6.910(-7)	1300.40
¹³ CO	J=2-1	15.87	6.038(-7)	1360.23
C ¹⁸ O	J=2-1	15.81	6.011(-7)	1365.42
CO	J=3-2	33.19	2.497(-6)	866.96
¹³ CO	J=3-2	31.73	2.181(-6)	906.84
C ¹⁸ O	J=3-2	31.61	2.172(-6)	910.31
CO	J=18-17	944.97	5.695(-4)	144.78
CO	J=36-35	3668.78	3.638(-3)	72.84
CO	v=1-0 J=3-4	3116.70	1.950(1)	4.699950
CO	v=1-0 J=35-36	6523.52	1.407(1)	5.040484
CO	v=2-1 J=3-4	6162.10	3.745(1)	4.758863
OI	³ P ₁ - ³ P ₂	227.712	8.91(-5)	63.18
OI	³ P ₀ - ³ P ₁	326.579	1.750(-5)	145.53
OI	¹ D ₂ - ³ P ₂	22830.18	6.535(-3)	0.63003
OII	² P _{3/2} - ² P _{1/2}	91.21	2.300(-6)	157.74
CI	³ P ₁ - ³ P ₀	23.620	7.880(-8)	609.14
CI	³ P ₂ - ³ P ₁	62.462	2.650(-7)	370.42
NeII	² P _{1/2} - ³ P _{3/2}	1122	8.59(-3)	12.815
NeIII	³ P ₁ - ³ P ₂	924.98	5.97(-3)	15.555
SII	² D _{5/2} - ⁴ S _{3/2}	21420	3.338(-4)	0.67164
SIII	³ P ₂ - ³ P ₁	1199.904	2.07(-3)	18.716
ArII	² P _{1/2} - ² P _{3/2}	2059.72	5.3(-2)	6.985
ArIII	³ P ₀ - ³ P ₁	2259.2	5.19(-3)	21.816
FeII	⁶ D _{9/2} - ⁶ D _{7/2}	553.6	2.13(-3)	25.988
SiII	² P _{1/2} - ² P _{3/2}	413.21	2.132(-4)	34.807
OH	² Π _{1/2} 7/2 ⁺ -5/2 ⁻	617.9	1.012	71.22
OH	² Π _{1/2} 7/2 ⁻ -5/2 ⁺	617.6	1.014	71.17
OH	² Π _{1/2} 1/2 ⁻ - ² Π _{3/2} 3/2 ⁺	181.9	3.606(-2)	79.11
OH	² Π _{1/2} 1/2 ⁺ - ² Π _{3/2} 3/2 ⁻	181.7	3.598(-2)	79.18
OH	² Π _{3/2} 5/2 ⁻ -3/2 ⁺	120.7	1.388(-1)	119.23
OH	² Π _{3/2} 5/2 ⁺ -3/2 ⁻	120.5	1.380(-1)	119.44
o-H ₂ O	1 ₁₀ -1 ₀₁	61.0	3.458(-3)	538.29
o-H ₂ O	2 ₁₂ -1 ₀₁	114.4	5.593(-2)	179.53
o-H ₂ O	4 ₂₃ -3 ₁₂	432.2	4.838(-1)	78.74
o-H ₂ O	8 ₁₈ -7 ₀₇	1070.7	1.751	63.32
p-H ₂ O	1 ₁₁ -0 ₀₀	53.4	1.842(-2)	269.27
p-H ₂ O	4 ₁₃ -4 ₀₄	396.4	3.726(-2)	187.110
p-H ₂ O	3 ₂₂ -2 ₁₁	296.8	3.524(-1)	89.988
o-H ₂	v=0-0 S(1) J=3-1	1015	4.76(-10)	17.034
p-H ₂	v=0-0 S(2) J=4-2	1682	2.754(-9)	12.278
p-H ₂	v=0-0 S(4) J=6-4	3474	2.642(-8)	8.025
o-H ₂	v=0-0 S(9) J=11-9	10262	4.898(-7)	4.694
o-H ₂	v=2-1 S(1) J=3-1	12550	4.977(-7)	2.248
p-H ₂	v=1-0 S(0) J=2-0	6472	2.526(-7)	2.223
o-H ₂	v=1-0 S(1) J=3-1	6952	3.471(-7)	2.122
CN	N=2-1 J=5/2-3/2	16.34	1.143(-4)	1321.380
CN	N=5-4 J=11/2-9/2	81.64	2.027(-3)	528.78
HCN	J=3-2	25.52	8.3559(-4)	1127.521
HCN	J=4-3	42.53	2.054(-3)	845.66
CH ⁺	J=2-1	120.195	4.760(-2)	179.594
CH ⁺	J=4-3	400.086	0.3781	90.011
CH ⁺	J=5-4	599.524	0.7346	72.137
HCO ⁺	J=1-0	4.28	4.2512(-5)	3361.334
HCO ⁺	J=3-2	25.68	1.4757(-3)	1120.478
HCO ⁺	J=4-3	42.80	3.6269(-3)	840.380
N ₂ H ⁺	J=3-2	26.83	1.2586(-3)	1072.558

Notes. The notation $x(-y)$ stands for $x \cdot 10^{-y}$.

¹ Self-shielding is taken into account using the approach described in Voitke et al. (2009a).

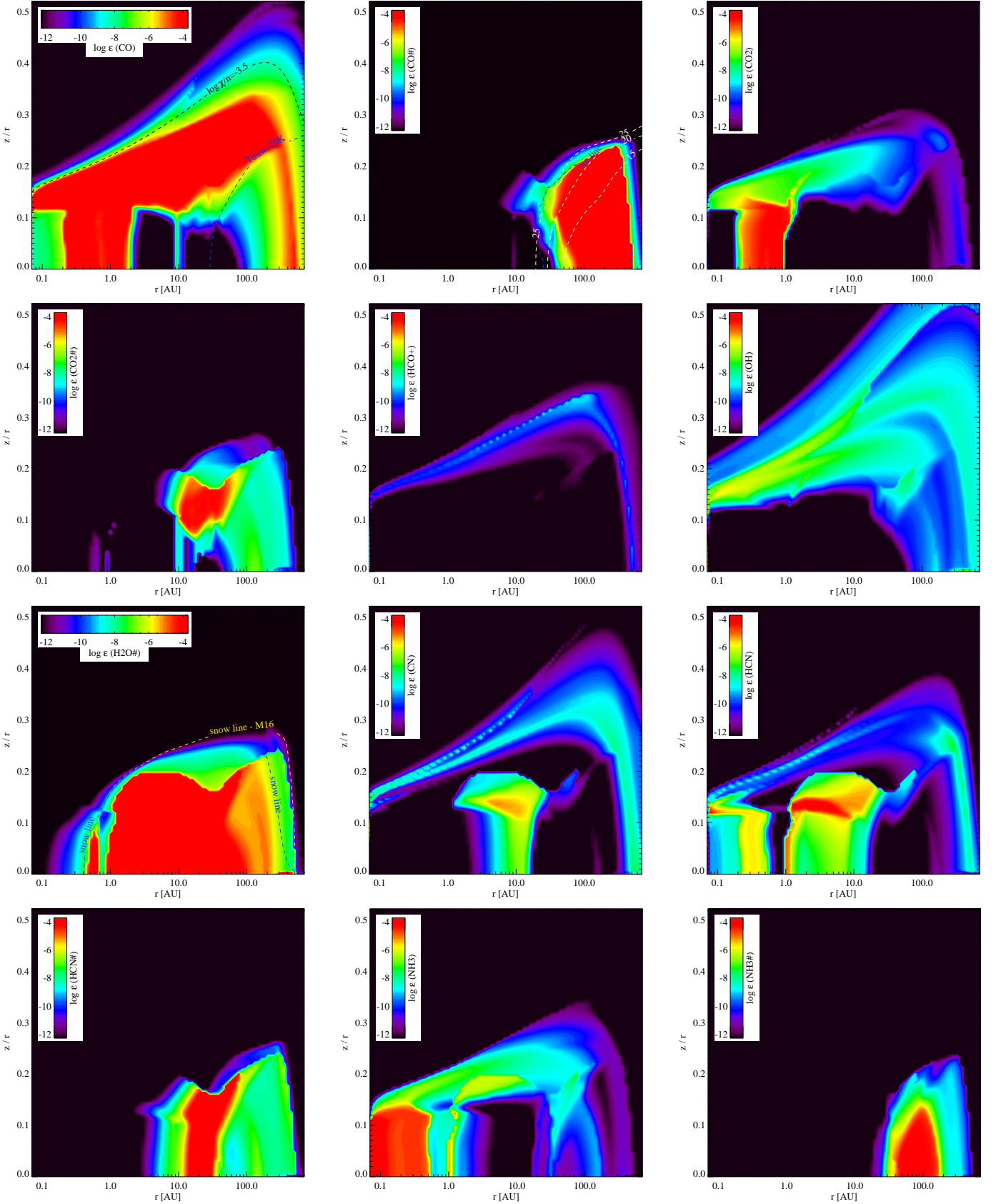


Fig. 1. Distribution of key species abundances in the base model: CO, CO#, CO₂, CO₂#, HCO⁺, OH, H₂O#, CN, HCN, HCN#, NH₃, NH₃#. For CO, the black contour shows the PDR parameter $\log \chi / \langle n_{\text{H}} \rangle = -3.5$ and the blue contour $T_{\text{dust}} = 20$ K where CO starts to freeze out on dust grains. For CO#, the white dashed contours show dust temperatures of 15, 20 and 25 K and the blue dashed line shows the CO ice line estimate from rate equilibrium (Antonellini 2016). For water ice, two approximations of the snow line are indicated: (1) Estimate based on the local density, dust temperature and radiation field (Min et al. 2016a, yellow dashed) and (2) Estimate from rate equilibrium (Antonellini 2016, blue dashed).

3.2. Chemical rates from UMIST2006 to 2012

The revision of the UMIST database in 2012 reveals major differences in species masses especially for nitrogen bearing species. The main reason is the missing collider reactions with respect to the UMIST2006 rate file. Fig. 2 shows this effect for the species that change by more than a factor three and have absolute masses above $10^{-15} M_{\odot}$. Species not shown here vary by less than a factor three.

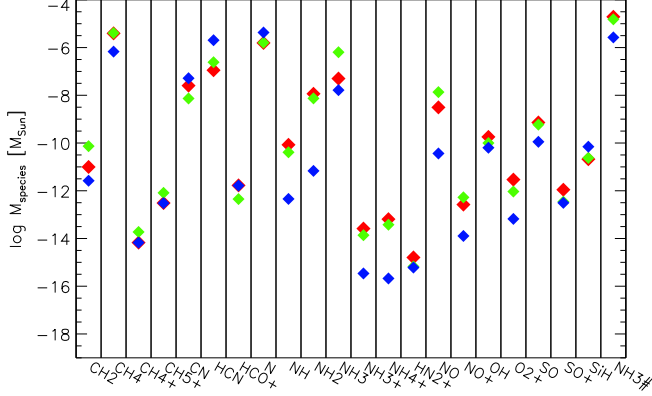


Fig. 2. Differences in species masses between three different sets of reactions: UMIST2012 plus collider reactions from UMIST2006 (red, model 1), UMIST2006 (green, model 2) and UMIST2012 (blue, model 1a).

In the case of UMIST2012 without the collider reactions, water and OH abundances in the surface of the outer disk change by orders of magnitude; in fact, the entire water vapor reservoir on top of the water ice reservoir disappears (Fig. 3). This is also reflected in the water and OH line fluxes changing by a factor 3-10 (Fig. 4). The rates were not deliberately omitted, but simply not re-assessed in UMIST2012, hence the UMIST2006 collider reactions should be used (Millar, private communication). Adding the collider reactions brings back the water and OH reservoir and also leads to a match of the water and OH line fluxes to within a factor 2-3 (Fig. 5). The three-body (collider) reaction opening the water formation pathway is



with a reaction rate of $10^{-26} \text{ cm}^6 \text{ s}^{-1}$ (Avramenko & Krasnenkov 1966). The rate is constant over the temperature range 564 – 796 K according to NIST. Since we extrapolate rates outside the temperature range, it gets applied also in the somewhat cooler disk surface regions (20 – 300 K). This rate stems from a very old measurement and definitely needs to be revisited. NH_2 subsequently reacts with oxygen to form NH and OH . Both radicals react further to form water (Kamp et al. 2013). The more classical neutral-neutral pathway identified e.g. by Glassgold et al. (2009)



acts at higher gas temperatures ($T_{\text{gas}} \gg 200 \text{ K}$) closer to the star.

CN , OH and HCO^+ show differences in species mass of up to 0.5 dex between UMIST2006 and UMIST2012 (plus collider reactions). Lines of these species are frequently observed in the far-IR and submm wavelength range and their predicted line fluxes can differ by up to a factor 2.5 for CN and OH and up

to a factor six for HCO^+ , with UMIST2012 giving systematically higher fluxes (Fig. 5). Throughout the remainder of this paper, we use ‘UMIST2012’ as a replacement for ‘UMIST2006’ rate database including the collider reactions’.

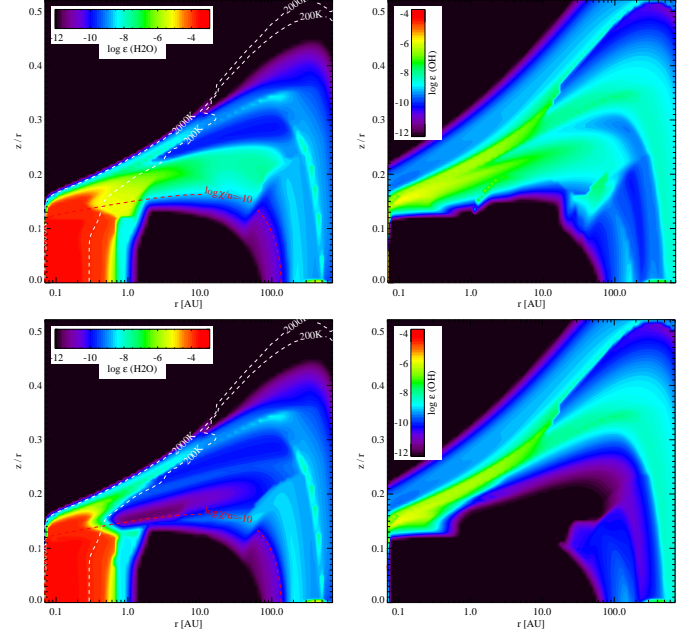


Fig. 3. Comparison of water and OH abundances in the UMIST2012 model with (top, model 1) and without collider reactions (bottom, model 1a).

3.3. Chemical reaction databases

We test the impact of different sets of reaction rates on the overall disk chemistry and appearance. Three databases are investigated: UMIST2012 (model 1), OSU (model 3) and KIDA (model 4). In all cases, we use the small chemical network and the adsorption energies of Aikawa et al. (1996a). We also keep the physical and thermal structure of the underlying disk constant.

Given that these databases have been compiled with different focus, it is not surprising that almost one third of the species masses change by more than 0.5 dex. In addition, collider reactions are not a priori included in these databases; hence water and OH are affected in the same way as described in Sect. 3.2. Fig. 6 provides an overview of a few key species for OSU and KIDA and can be compared to Fig. 1 and 3.

However, despite these large changes in the overall chemical structure, some line tracers stay very robust while others change by more than 1 dex (see Figs. 7 and 8):

- The low excitation CO lines hardly change. This is due to the simple molecular cloud like chemistry in the outer disk. However, there are significant changes in the high excitation rotational lines and ro-vibrational lines that originate in the inner 10 au where CO chemistry is driven by ion-molecule and in lower layers by neutral-neutral reactions. Interestingly, OSU gives systematically higher fluxes, while KIDA is lower than UMIST2012. This relates to the depth at which the $\text{C}^+/\text{C}/\text{CO}$ transition is reached in those different networks. Self-shielding is treated in the same way for all three networks. The main CO formation reactions are via OH producing CO^+ . The OH radical can

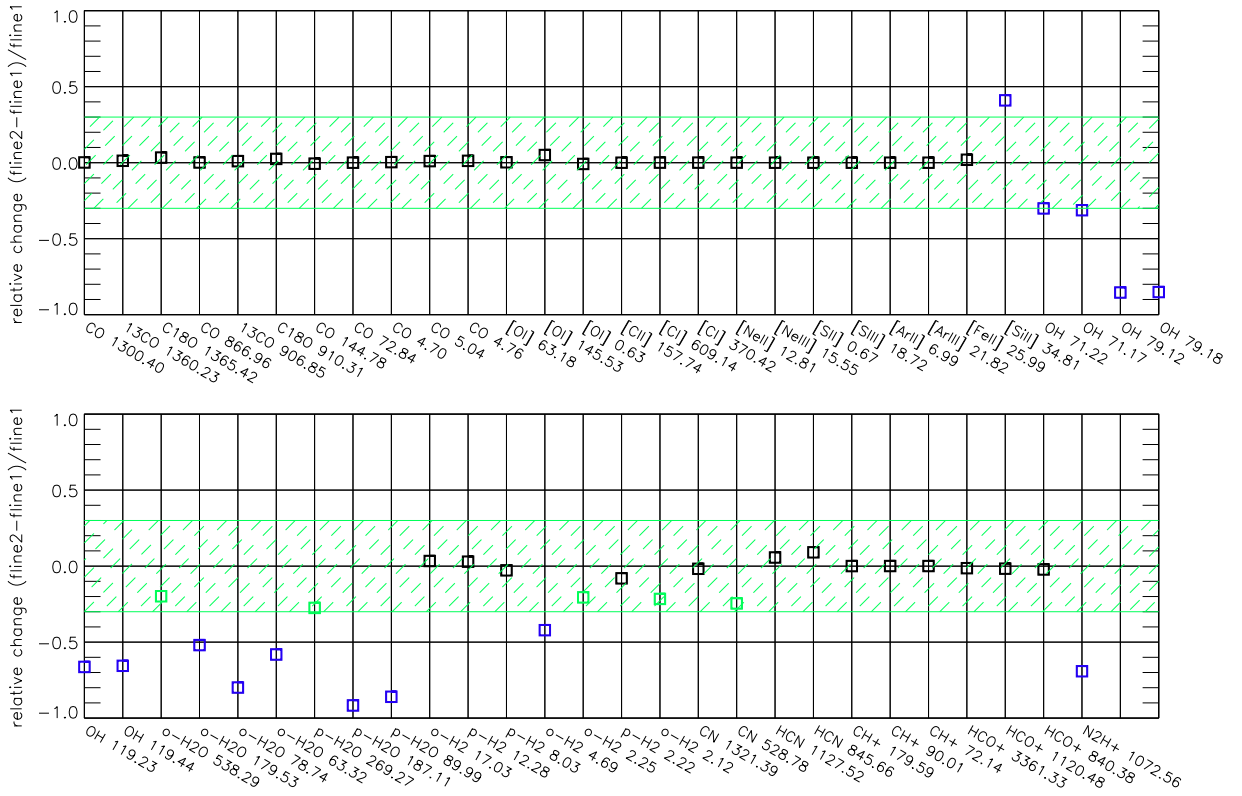


Fig. 4. Comparison of line fluxes for two sets of reactions: UMIST2012 plus CL reactions from UMIST2006 (fline1, model 1) and UMIST2012 (fline2, model 1a). Black and green squares denote differences of less than 25% and less than a factor two respectively, blue squares and red triangles denote differences larger than a factor three and ten respectively.

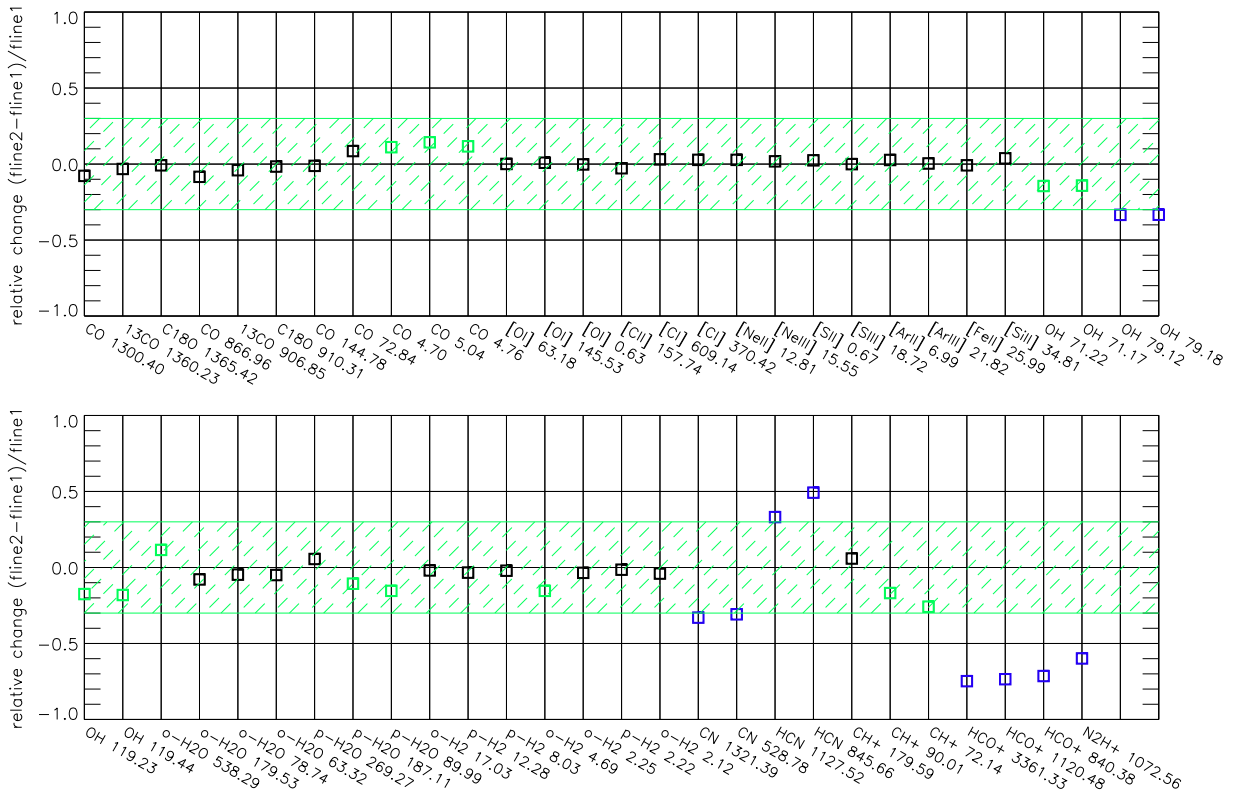


Fig. 5. Comparison of line fluxes for two sets of reactions: UMIST2012 plus CL reactions from UMIST2006 (fline1, model 1) and UMIST2006 (fline2, model 2). Black and green squares denote differences of less than 25% and less than a factor two respectively, blue squares and red triangles denote differences larger than a factor three and ten respectively.

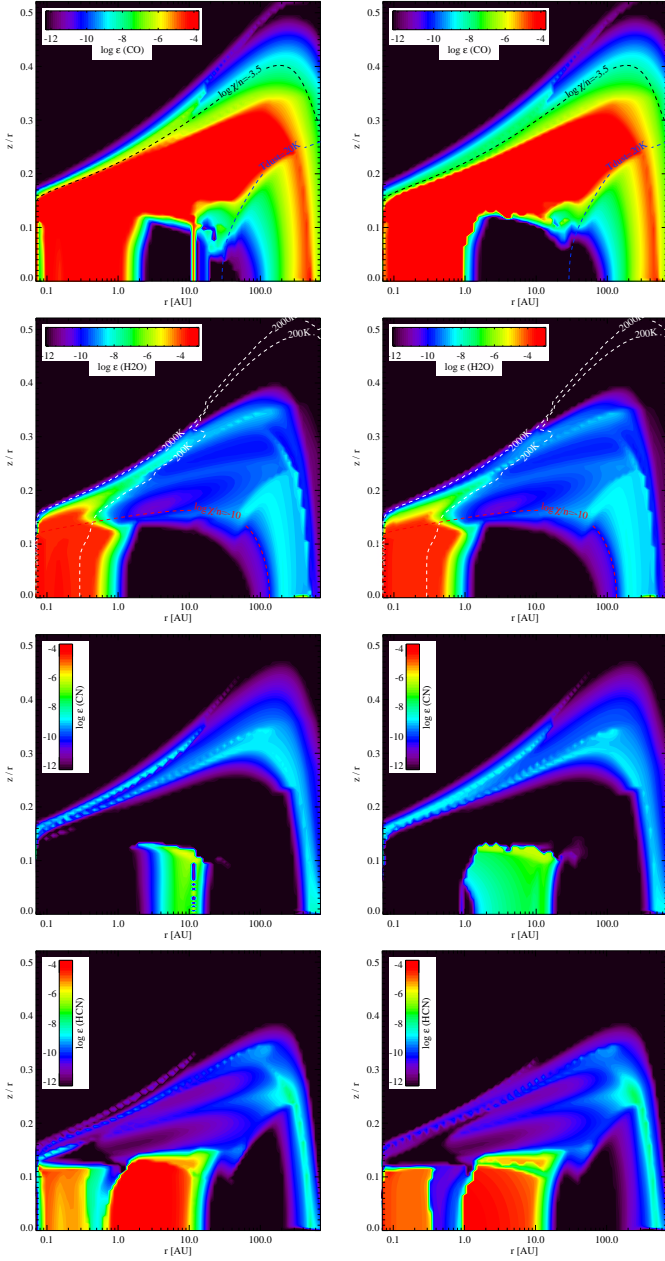


Fig. 6. Distribution of key species abundances using OSU (left) and KIDA (right): CO, H₂O, CN, HCN. Contours are the same as those in Fig. 1 and 3.

react with H₂, N or C⁺ and the latter forms CO⁺ (OH + C⁺ → CO⁺ + H). Subsequent reactions with H and H₂ lead to CO (CO⁺ + H → CO + H⁺ and CO⁺ + H₂ → HCO⁺ + H followed by HCO⁺ + e → CO + H). Reaction rates for these differ between the networks. Apparently, even small rate differences can lead to significant differences in line fluxes. The transition lies closest to the surface in the OSU model, while it lies deepest in the KIDA model (see Fig. 1 and 6); note that the CO high excitation lines react very strongly to changes in temperature and the C⁺/C/CO transition has a steep vertical temperature gradient.

- The neutral and ionized atomic line fluxes are very robust and stay within a factor two across all networks; those species are dominated by photochemistry and their abundance (and line flux) directly reflects the choice of elemental

Table 7. Comparison of rate coefficients for CH⁺ formation and destruction reactions.

Reaction	KIDA 2011			UMIST 2012		
	A	B	C	A	B	C
C + H ₃ ⁺	2(-9)	0.0	0.0	2.00(-9)	0.0	0.0
C ⁺ + H ₂	7.8(-10)	0.0	4540.0	1.00(-10)	0.0	4640.0
CH ⁺ + H ₂	1.20(-9)	0.0	0.0	1.20(-9)	0.0	0.0
CH ⁺ + e	7(-8)	-0.5	0.0	1.50(-7)	-0.42	0.0

Notes. The coefficients A, B and C have their usual meaning (see e.g. McElroy et al. 2013). The notation $x(-y)$ denotes $x \cdot 10^y$.

abundances.

- H₂ chemistry is driven by formation on dust and photodissociation; these processes are implemented outside the specific network. A crucial reaction in the inner disk destroying H₂ is collisions with atomic oxygen, leading to the formation of OH. The rate constants do not differ much in the three networks

UMIST – $A = 3.14 \cdot 10^{-13}$, $B = 2.7$, $C = 3150$ (297-3532 K)

OSU – $A = 3.44 \cdot 10^{-13}$, $B = 2.67$, $C = 3160$ (1-40000 K)

KIDA – $A = 3.44 \cdot 10^{-13}$, $B = 2.67$, $C = 3160$ (10-280 K)

However, for the reactions consuming OH, the rate coefficients are different in the three networks, propagating into the OH abundances in the surface layers inside 10 au. Emission lines of molecular hydrogen turn out to be mostly within a factor 3. Many of the H₂ lines discussed here originate in a thin surface layer limited in depth by the dust continuum. The high rotational line at 4.694 μm as well as the ro-vibrational lines are optically thin similar to what was found by Nomura & Millar (2005). This makes line flux predictions very sensitive to the exact placement of the H/H₂ transition in the disk model.

- HCN lines originating in the outer disk are also very robust; again, similar to the CO case, the chemistry here is largely molecular cloud chemistry.
- CN outer disk abundances are lower in the OSU and KIDA disk models (see Fig. 1 and 6) and the corresponding lines originating in the outer disk are systematically weaker for those networks compared to UMIST2012. One difference in the networks is the CN destruction reaction with oxygen, which is a factor ~ 2 stronger in OSU and KIDA at low temperatures compared to UMIST2012.
- OH and water lines differ within a factor 10 between the OSU/KIDA and UMIST2012. This is mainly due to the missing collider reactions that affect the outer lower reservoirs of these two molecules.
- The largest differences (more than one order of magnitude) are seen in line fluxes of CH⁺ between UMIST2012 and KIDA. This is due to differences in reaction rates leading to the formation and destruction of this radical (see Table 7).

3.4. Adsorption energies

After having seen differences arising from different networks, we focus now on adsorption energies that affect the gas/ice reser-

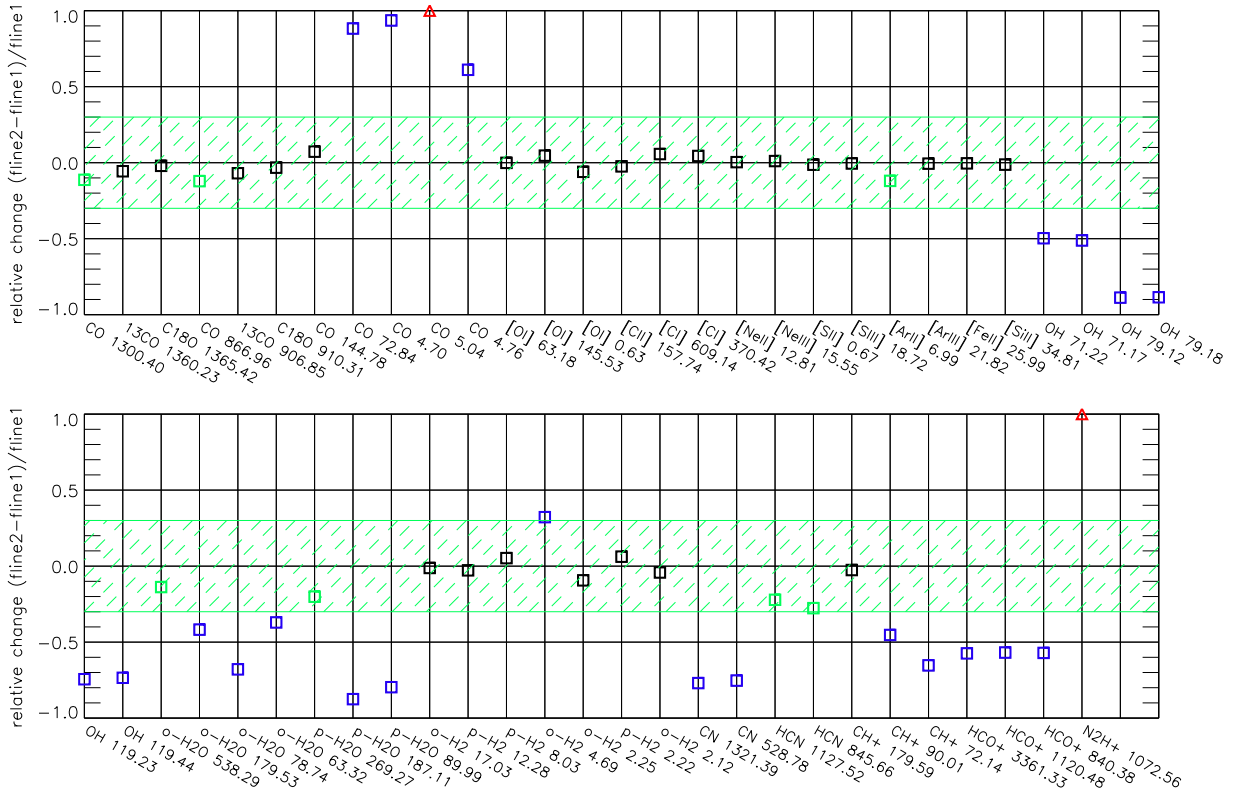


Fig. 7. Comparison of line fluxes for two databases: UMIST2012 (fine1, model 1) and OSU (fine2, model 3). Black and green squares denote differences of less than 25% and less than a factor two respectively, blue squares and red triangles denote differences larger than a factor three and ten respectively.

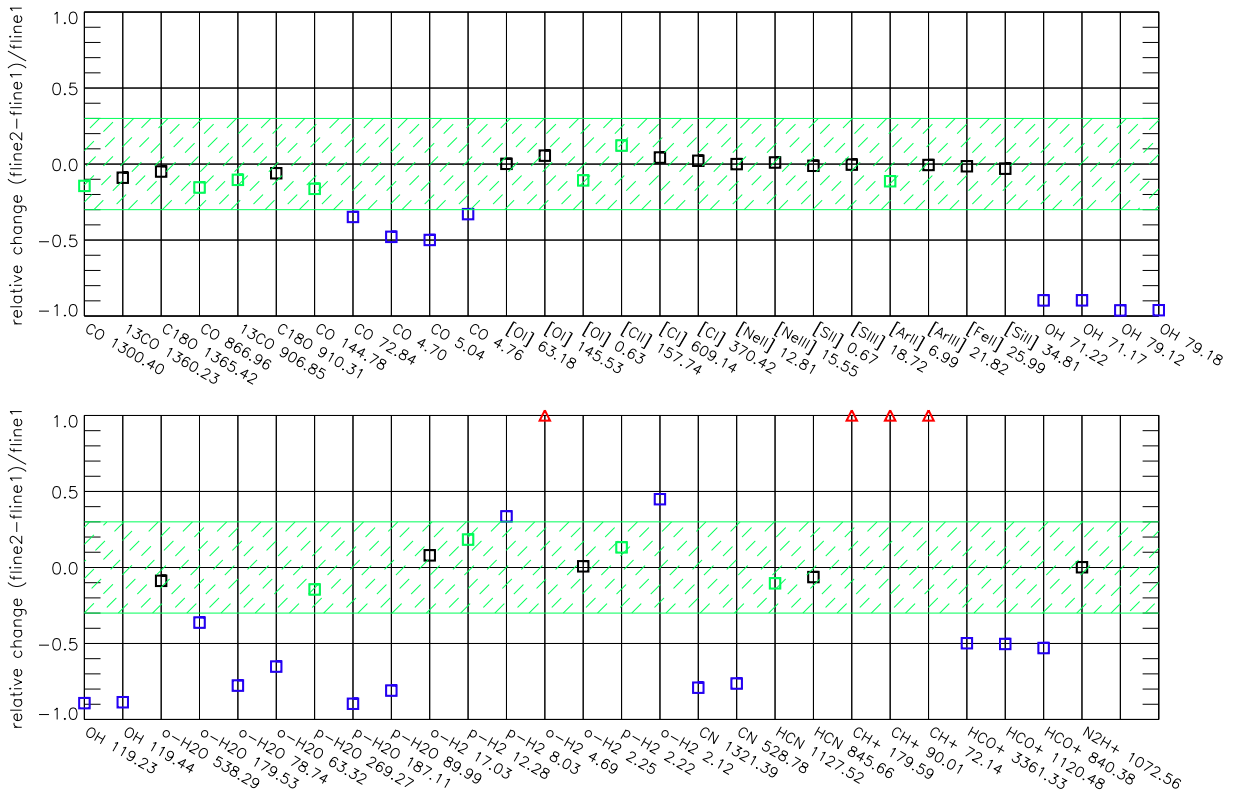


Fig. 8. Comparison of line fluxes for two databases: UMIST2012 (fine1, model 1) and KIDA (fine2, model 4). Black and green squares denote differences of less than 25% and less than a factor two respectively, blue squares and red triangles denote differences larger than a factor three and ten respectively.

voirs in the disk. Collings et al. (2004) found for example that CO can be trapped in the polar water ice at much higher temperatures than in a non-polar CO ice. The dependence of chemical abundances on the specific grain surface — SiO₂, polar, non-polar — has already been noted by Bergin et al. (1995). Here, we explore systematically the effects of using different sets of adsorption energies and explore a first simple model that illustrates the effect of surface dependent adsorption energies.

The thermal desorption rate of a species i depends among other variables also on the adsorption energy $E_{\text{ads}}(i)$ (expressed in K)

$$R = n_{\#} v_{\text{osc}}(i) \exp\left(-\frac{E_{\text{ads}}(i)}{T_{\text{dust}}}\right) \text{ cm}^{-3} \text{ s}^{-1}, \quad (3)$$

where $v_{\text{osc}}(i)$ is the oscillation frequency of species i , $n_{\#}$ the density of desorbable species i on the grain surface², and T_{dust} the temperature of the grain. The oscillation frequency depends only weakly on the adsorption energy of the species, thus making the exponential term in Eq. (3) the dominant one.

Adsorption energies measured in experiments differ largely depending on whether they are measured from ice on top of the same ice, ice mixtures or ice on bare graphite or silicate grains. Fig. 9 shows two examples for values collected for NH₃ and HCN ice. The set of adsorption energies from Aikawa et al. (1996a) corresponds to bare carbonaceous or silicate surfaces. Alternatively, Garrod & Herbst (2006) compiled a set of adsorption energies that is valid for non-porous water ice surfaces. Fig. 9 shows that most values found in the literature indeed group around either the low bare grain value or the higher value on water ice. Values for the adsorption of a species on its own ice reside somewhere in between (see e.g. NH₃ vapor enthalpy and NH₃ on ammonia ice, Sandford & Allamandola 1993). UMIST2012 recommends a set of adsorption energies that largely agrees (within 30%) with Garrod & Herbst (2006). The only exception among the species in common is HCOOCH₃ (GH06: $E_{\text{ads}} = 6300$ K, UMIST2012: $E_{\text{ads}} = 4000$ K). A more general overview of the uncertainties around adsorption energies and a critical review can be found in Cuppen et al. (2017). We compare in the following three sets of adsorption energies: Aikawa et al. (1996a) (model 1), Garrod & Herbst (2006) (model 5) and UMIST2012 (model 6).

Differences in the adsorption energies affect most species masses by less than a factor 2-3. However, a few species change by more than a factor 3, some even by an order of magnitude: CN, HCN, CO₂, NH₂, N₂, N₂H⁺, Si, SiH, and HCN ice (Fig. 10). The extent of the various ice reservoirs changes from one set of adsorption energies to the other (see Fig. 12). The most extreme case is NH₃ ice where the ice line moves from 40 au (E_{ads} from Aikawa et al. 1996a) to 0.3 au (E_{ads} from Garrod & Herbst 2006). Note that a significant change in the ice line does not have to lead to a significant change of the species mass and thus the two provide complementary information. We discuss in the following the processes behind the changes in the chemistry.

- CO₂: The snow line limits the radial extent of the CO₂ ring in the midplane of the disk, where water is not yet completely frozen onto the cold dust grains. The snow line changes from ~ 1 au to ~ 0.3 au for the two different values of E_{ads} for water, 4800 K and 5700 K. However, none of this affects the water ice reservoir since that is dominated by the

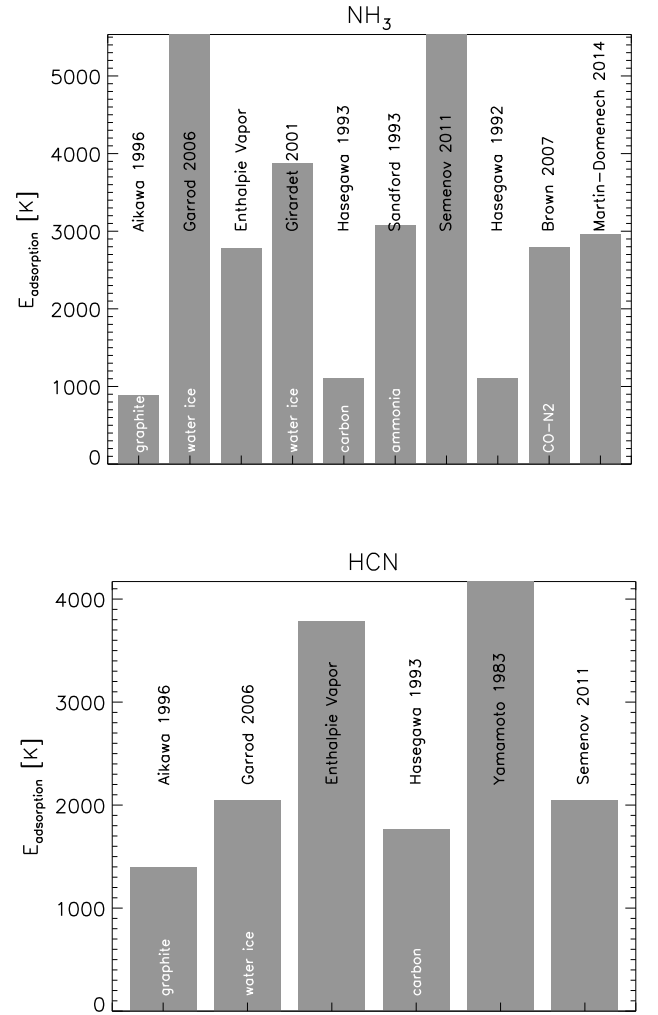


Fig. 9. Comparison between various literature values for the adsorption energy of NH₃ and HCN. White text indicates the surface on which the adsorption energy was measured, so bare carbonaceous grains, ammonia ice, water ice or an ice mixture; black text are the references.

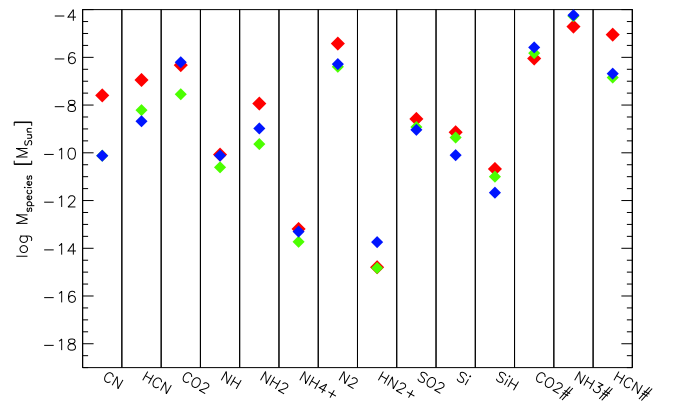


Fig. 10. Differences in species masses between three different sets of adsorption energies: Aikawa et al. (1996a) (red, model 1), Garrod & Herbst (2006) (green, model 5) and McElroy et al. (2013, UMIST2012) (blue, model 6). Shown are only species that differ by a factor three or more.

² Details on the various thermal and non-thermal desorption processes can be found in Woitke et al. (2009a).

Table 8. Adsorption energies used in the two temperature regimes: bare grains and polar ices.

ice species	E_{ads} [K]			
	$T > 110$ K	Ref.	$110 \leq T \leq 10$ K	Ref.
CO	960	A96	1150	UMIST2012
H ₂ O	4800	H09	5700	GH06
CO ₂	2000	A96	2990	UMIST2012
CH ₄	1360	HH93	1090	UMIST2012
NH ₃	880	A96	3874	G01
SO ₂	2400	A96	5330	UMIST2012
O ₂	960	as CO	1000	UMIST2012
HCN	1400	A96	2050	UMIST2012
N ₂	660	scaled CO	1870	G01

Notes. Abbreviations for references can be found in Table A.1.

mass in the outer disk.

- *CN, HCN, NH₂, N₂*: The adsorption energy of NH₃ ice determines the radial ice line for this species. For $E_{\text{ads}} = 880$ K (Aikawa), the NH₃ ice reservoir extends from 40 to 200 au and nitrogen does not fully condense into NH₃ ice. For $E_{\text{ads}} = 5530$ K (GH06, UMIST2012), all nitrogen is bound in NH₃ ice between 0.3 and 200 au. With a low adsorption energy, sufficient nitrogen remains in the gas phase between 1 and 10 au to form CN, HCN, NH₂, and N₂. Fig 10 shows that all these species have lower masses in case of the higher adsorption energy (GH06, UMIST2012), while the mass of NH₃ ice increases by a factor three.
- *N₂H⁺*: The ice line for several ice species, particularly also CO, shifts upward beyond 20 au, if the UMIST2012 adsorption energies are used instead of the Aikawa et al. (1996a) ones. This increases the abundance of N-bearing species in the region which is oxygen poor. Since N₂H⁺ resides in a thin layer at the disk surface, this extra reservoir causes an increase in mass by a factor ~ 10 .
- *Si, SiH*: The change in the mass of Si and SiH is related to CO₂. In models with a low adsorption energy for water, the CO₂ ring is extended out to a few AU. In this ring, CO₂ reacts with Si to form SiO which subsequently freezes out onto the cold dust grains, driving Si into SiO ice at the expense also of the SiH abundance. In the models with a high adsorption energy, Si remains atomic out to a few au. The SiO that forms is efficiently destroyed by reactions with C⁺ into Si⁺ which is then subsequently neutralized by charge exchange with Mg and Na.

Despite the fact that several gas species masses change drastically, none of the lines studied here is affected by more than a factor 2 except the N₂H⁺ line (Fig. B.1 and B.2). Most of the lines are optically thick and/or originate in the disk surface and do not trace the chemistry changes occurring typically closer to the midplane. The only lines changing by a factor 2 are the optically thin lines of C¹⁸O (1365.42 and 910.31 μm), and the CN line (528.78 μm). The N₂H⁺ line at 1072.56 μm increases by more than a factor 10 if the UMIST2012 adsorption energies are used; this is related to the increase in N₂H⁺ mass as shown in Fig. 10 due to the change in N₂ adsorption energy (GH06: 1000 K, UMIST: 790 K). Apart from the line flux changes, Fig. 11 shows that the N₂H⁺ density distributions and therefore also emitting regions in the disk change depending on the set of adsorption energies used.

It is reasonable to assume that the adsorption energy of a specific molecule will depend on the surface property of the grain, i.e. bare surfaces and/or the polarity of the ice. Hence, we ran an additional model in which we vary the adsorption energy as a function of temperature (model 7). For that we assume two temperature intervals: (1) bare grain surface values for $T > 110$ K, and (2) polar ice values for $110 \text{ K} \leq T \leq 10$ K. Table 8 summarizes the values and regimes for the ices used in the small chemical network. The N₂ adsorption energy is now scaled by a factor 0.7 with respect to the one by Aikawa et al. (1996a); such a scaling has already been proposed by Bergin & Langer (1997). Ceccarelli & Dominik (2005) show that such a scaling is required to match H₂D⁺ observations and Rab et al. (in preparation) show that it matches typical N₂H⁺ line fluxes from disks. Again, the disk density and thermal structure is kept constant.

Fig. 13 shows the change in species masses with respect to the Aikawa adsorption energy set for those species that change by a factor three or more: CN, HCN, CO₂, NH, NH₂, NH₄⁺, N₂, N₂H⁺, O₂⁺, SO, CO₂ ice, NH₃ ice and HCN ice. The species masses of the temperature-dependent case sometimes follow the bare grain case and sometimes the water ice surface case. Species with high abundances in the inner disk such as CO₂ stay close to the results from bare grains since this is in fact the adsorption energy that governs their behavior in the temperature-dependent case. Most other species stay close to the results from water ice surfaces since they are dominated by the behavior in the outer disk where grains are covered by water ice. A few species deviate from this, N₂H⁺, O₂⁺ and SO. In these three cases, the temperature dependent adsorption energies always yield smaller species masses than any of the other two models. This is related to the higher value of N₂ adsorption energy in the temperature range $110 \leq T \leq 10$ K (Girardet & Toubin 2001, on water ice), which allows nitrogen to deplete from the gas phase at smaller radii than in the other two models. This impacts many nitrogen bearing species, but also those which form through nitrogen chemistry including for example gas phase water beyond 10 au.

None of the lines in our selection changes by more than a factor two with respect to the bare grain case (Aikawa et al. 1996a) except the N₂H⁺ line (see Fig. B.3). The latter becomes a factor six weaker in the case of temperature-dependent adsorption energies. The largest changes in the chemical composition are seen in the ice reservoir inside 100 au (Fig. 12); however most lines originate well above the surface ice line.

3.5. Reactions of excited H₂

We discuss the compilation of reaction rates for excited H₂ (denoted throughout the rest of the paper as H₂^{*}) in Appendix A.4, where we assume a representative excitation state of $\nu = 1$ ($E = 5980$ K). It is assumed that 90% of the UV absorption leads to excited H₂, 10% to dissociation (Tielens & Hollenbach 1985).

We find from our standard model that the molecular ions CH⁺ and HCO⁺ are the most affected species. In both cases, the key reaction is



We use here the updated rate from Eq.(A.5) as explained in the Appendix. The mass of CH⁺ increases by a factor ~ 10 due to the presence of excited H₂ chemistry. All other species masses change by less than 10 %. The change in CH⁺ abundance transmits through various channels into CH₂⁺, CH₃⁺ and all

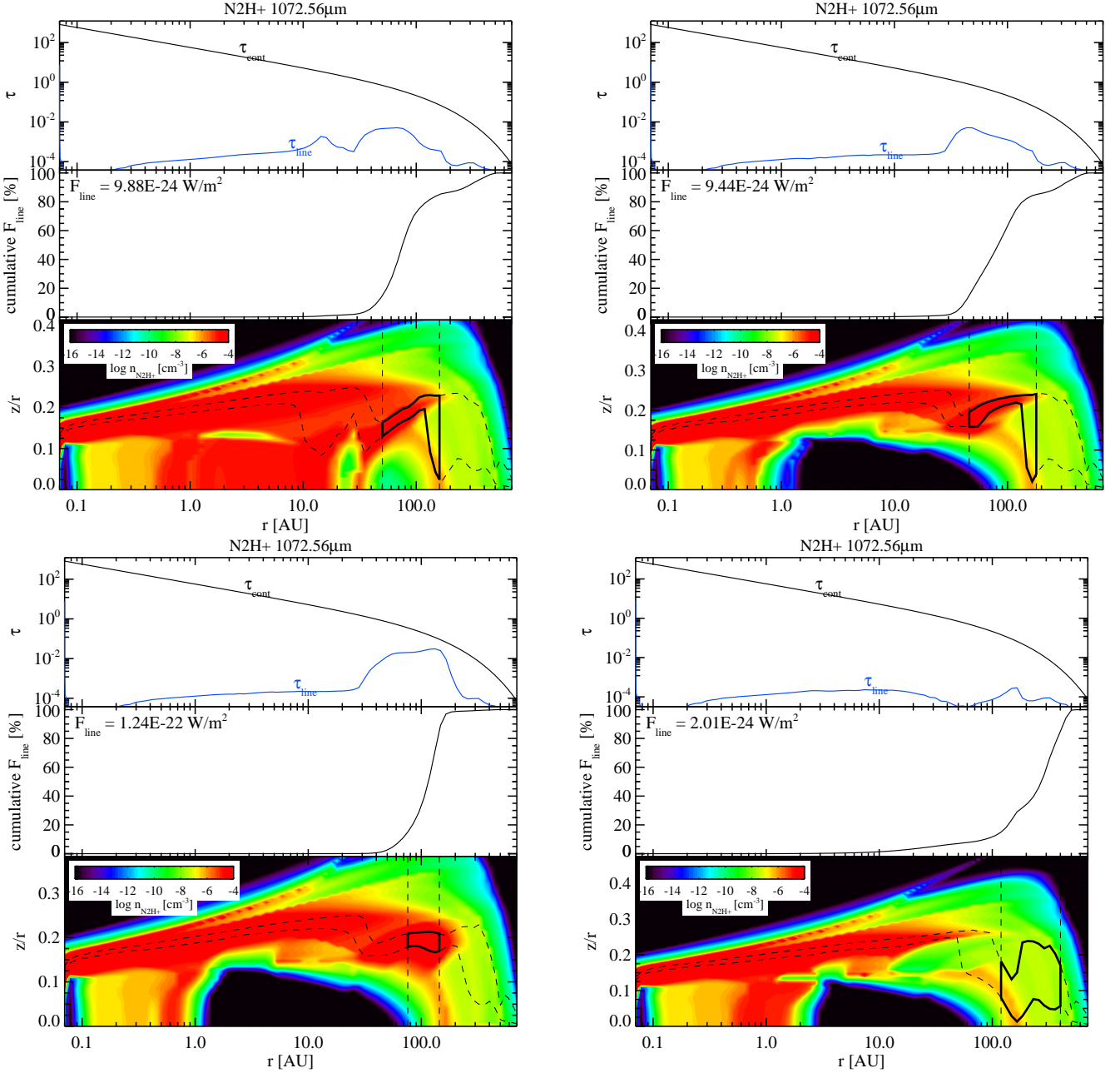


Fig. 11. N_2H^+ $J=3-2$ line ($1072.56\ \mu\text{m}$) from vertical escape for the four models from top left to bottom right: The standard disk model using the set of adsorption energies from Aikawa et al. (1996a) (model 1), Garrod & Herbst (2006) (model 5), UMIST2012 (model 6), T -dependent adsorption rates (model 7). The three panels show the optical depth in the line and the continuum, the cumulative line flux as a function of radius and the box (thick black line) in which 50% of the line flux originates (15-75% radially and vertically - dashed black lines) on the color background of the N_2H^+ density distribution.

those molecular ions have a pathway to form HCO^+



However, there are also many alternative pathways forming and destroying HCO^+ that do not involve H_2^+ . Hence, the species changes much less than CH^+ .

3.6. Large versus small networks

With the advent of ALMA, more complex molecular species and especially molecular ions will be detected in many more disks. Hence, we compare the use of small versus large networks. Again, we keep the disk density and thermal structure fixed and compare model 6 (100 species, 1288 reactions) to model 8 (235 species, 3167 reactions) using the UMIST2012 chemical database and adsorption energies.

Figures 14 and 15 show differences at the outermost radii due to the presence of more complex ices. Those affect also the outer water, HCO^+ and HCN reservoirs. Most of these changes

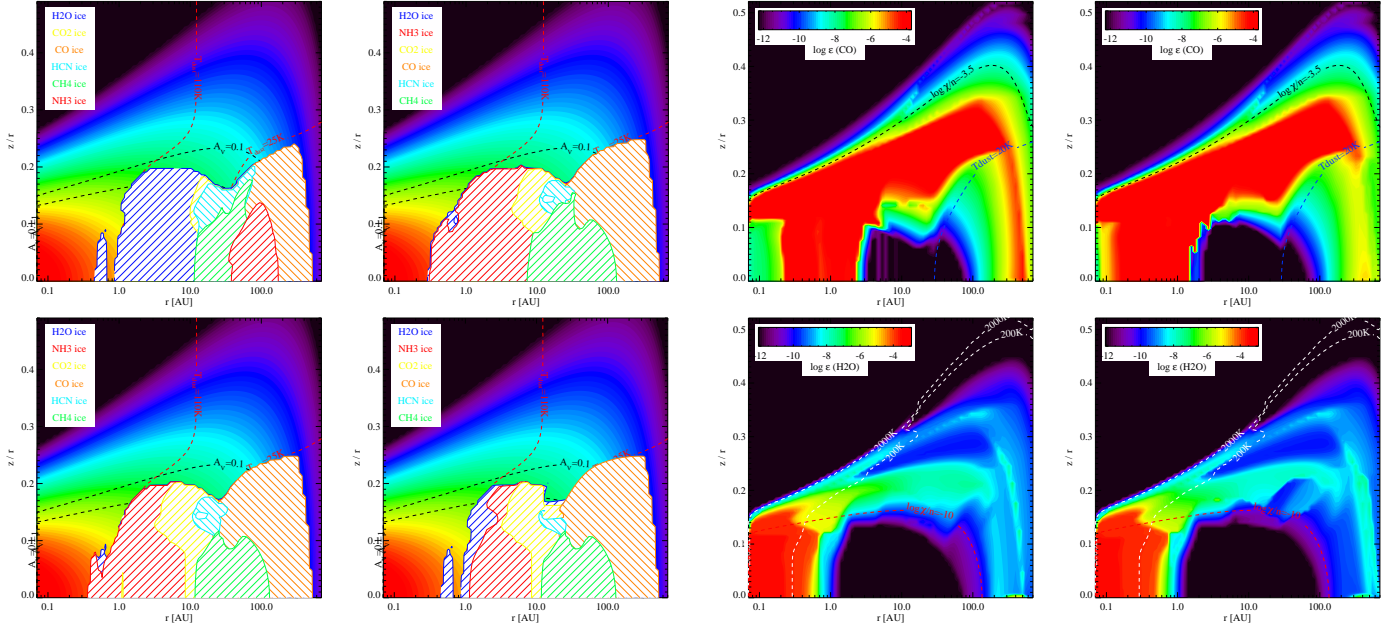


Fig. 12. Distribution of ice reservoirs plotted on top of each other in order from top to bottom of legend. Note that some ices may be partially hidden behind others. The order but not the color scheme is changed for the upper left panel to make the ammonia ice visible. From top left to bottom right: The standard disk model using the set of adsorption energies from Aikawa et al. (1996a) (model 1), Garrod & Herbst (2006) (model 5), UMIST2012 (model 6), T -dependent adsorption rates (model 7). The color scale in the background shows the total hydrogen number density in the disk model and the black dashed lines the $A_V = 0.1$ and 1 contours (minimum of radial and vertical A_V).

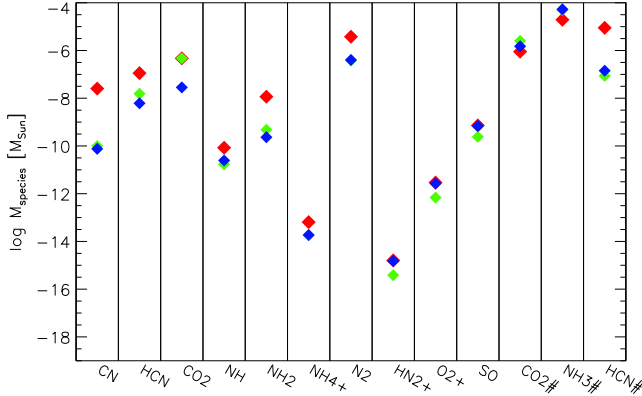


Fig. 13. Differences in species masses between E_{ads} of Aikawa et al. (1996a, red, model 1 - bare grains), temperature-dependent adsorption energies (green, model 7) and E_{ads} of Garrod & Herbst (2006, blue, model 5 - water ice).

come from new branches of chemistry allowed in the larger network such as C-chain chemistry (C_nH_m), more links between the nitrogen, oxygen and carbon chemistry networks through C-N and N-O bearing species, and sulphur chemistry. In addition, the presence of additional ices and PAHs (with their ice counterpart) changes the electron abundance in the disk. Hydrocarbons change in some cases by several orders of magnitude in species

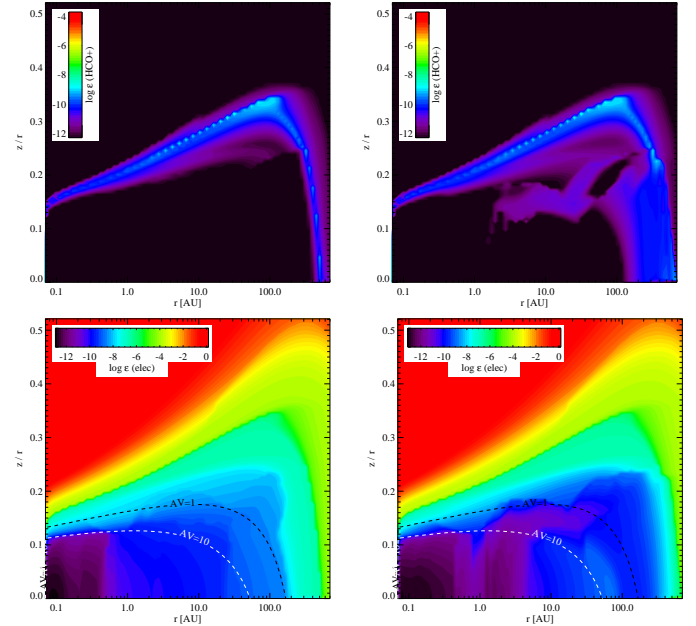


Fig. 14. Distribution of key species abundances using the small (left) and large (right) chemical network: CO, H₂O, HCO⁺, and electrons. Contours are the same as Fig. 1.

mass (e.g. CH₃, CH₄ and CH₅⁺ in Fig. 16). In addition, many hydronitrogens (azanes) change in mass between a factor three to ten (e.g. NH₂, NH₃⁺, NH₄⁺, N₂H⁺). Differences in molecular species mass beyond a factor 10 are also seen for H₃⁺ (~ 1.2 dex), NO⁺ (~ 1.3 dex), H₃O⁺ (~ 1 dex), SiH (~ 1.8 dex), and SiOH⁺ (~ 1 dex). Many metals and metal ions also change their species masses by more than a factor three. For the ices in common, the largest changes are seen in CH₄ ice (~ 1.8 dex), SO₂ ice (~ 1.4 dex) and HCN ice (~ 1.5 dex).

Fig. 17 reveals that the majority of lines investigated here do not change when we expand the chemical network to include more complex chemistry. Some lines change within a factor three, something easily buried in uncertainties within other disk input parameters; examples are the fine-structure lines of

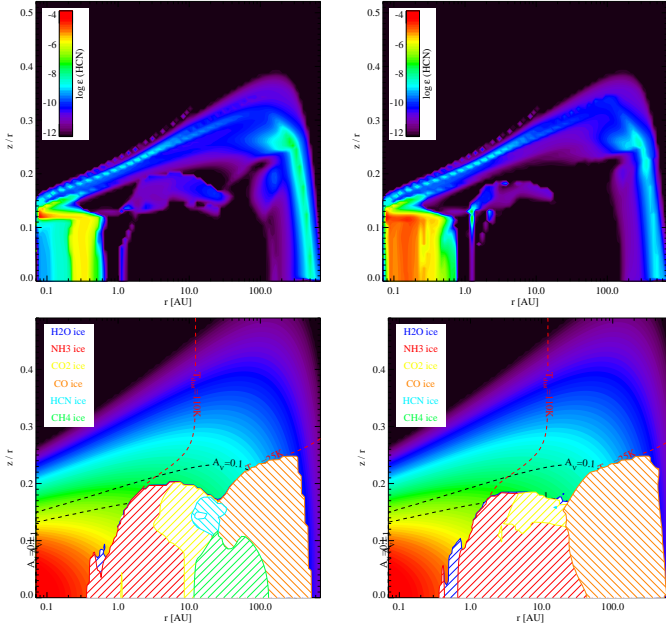


Fig. 15. Distribution of key species abundances using the small (left) and large (right) chemical network: HCN and ice reservoirs. Contours and legend are the same as Fig. 12.

neutral carbon at 609 and 370 μm . The sub-mm lines of HCN decrease in the larger network by more than a factor three.

HCO^+ and N_2H^+ lines increase by more than an order of magnitude when the larger network is considered. For HCO^+ , this is due to a decrease in electron abundance in the regions where this molecule can form (see Fig. 17), especially in the outer disk beyond 100 au. The change in electron abundance (see Fig. 14) is related to the freeze out of all neutral molecules and atoms (e.g. also sulphur and iron) included in the large network; the small network comprises only freeze-out of the molecules CO, H_2O , CO_2 , CH_4 , NH_3 , SiO, SO_2 , O_2 , HCN and N_2 . More chemical details behind these changes are explained in Rab et al. (2017) with the caveat that they only use the large chemical network.

4. Discussion

Most of the results outlined above are not specific to the choice of thermo-chemical disk code. We fixed the disk structure and exploited purely changes related to the choice of chemical database, set of adsorption energies and size of the network. Similar changes would show in any chemical code if it is applied to the large range of physical and irradiation conditions in disks. It has to be kept in mind that the chemical databases used in astrochemistry were originally developed for low density cold environments such as molecular clouds. Networks extending to higher temperatures more appropriate for inner disk regions have been developed (e.g. Agúndez et al. 2008; Harada et al. 2010), but are not routinely included in disk chemical models. With this work, we thus push the existing widely-used databases into regimes they have originally not been tested for.

Contrary to McElroy et al. (2013) we find large differences when comparing different chemical databases. We calculate the chemistry in environments of higher densities ($\geq 10^8 \text{ cm}^{-3}$) and temperatures (10 – 5000 K), while McElroy et al. (2013) used a dark cloud environment with $n(\text{H}_2) = 10^4 \text{ cm}^{-3}$, $T = 10 \text{ K}$, $A_V = 10 \text{ mag}$. Hence, we find differences both in the spatial

distribution of species and also in the resulting line fluxes. The differences for OH and water between UMIST and OSU/KIDA can likely be attributed to collider reactions. In addition, many lines originating from the inner disk show changes larger than a factor two. This indicates differences in the warm chemistry between the networks; abundances of many even simple molecules change in the inner disk where gas temperatures are in excess of a 300 K. These differences would not show up under the low density and low temperature conditions of a dark cloud.

The tests with different sets of adsorption energies shows that most atomic and molecular lines do not depend on these values. Many of these lines are optically thick and hence originate largely in the surface layers well above the ice reservoirs. However, the C^{18}O lines are optically thin and therefore directly linked to the size and height of the CO ice reservoir. The fluxes and emission maps of C^{18}O will depend on the details of how ices are treated within the chemical network. Another optically thin line is CN 528.78 μm . If adsorption energies from bare grains are used, the nitrogen reservoir changes significantly and the CN line has an additional contribution from regions inside 100 au. Yet another optically thin line is N_2H^+ . The emitting region and also column densities of this species depend crucially on the choice of N_2 adsorption energy and especially also the relative difference between CO and N_2 adsorption energies.

It has been shown by Agúndez et al. (2010) that reactions with excited H_2 play an important role in the formation of CH^+ in diffuse clouds and in Photon Dominated Regions (PDRs). The authors also point out the possible relevance to circumstellar disks. Our tests show now that state-to-state chemical reactions in disks affect indeed mostly CH^+ ; the effect on other molecular ions is minor. Hence for the interpretation of line fluxes and rotational diagrams of CH^+ such as presented in Thi et al. (2011a) and Fedele et al. (2013), it is important to take reactions with excited H_2 into account.

Semenov et al. (2004) found that especially the intermediate layers of disks where ion-molecule chemistry is active require larger chemical networks in excess of 100 species. However, they focussed largely on the ionization degree to inform MHD disk models and their model assumes that gas and dust temperatures are equal. The latter assumption leads to colder disk surface layers compared to our model. Many neutral-neutral reactions with barriers become only important for gas temperatures above 300 K. Our comparison between the small (100 species, 1288 reactions) and large (235 species, 3167 reactions) network shows the importance of additional freeze-out due to the presence of more ice species. As Semenov et al. (2004), we note the importance of carbon chain chemistry. The new chemical pathways opened by connecting C-N, N-O and sulphur chemistry affect the abundance distribution of species even in the outer disk. The emission lines affected by this are mostly HCN, N_2H^+ and HCO^+ , while the CO and CN lines stay within a factor ~ 2 . Hence, for the interpretation of submm maps and emission lines of HCN, N_2H^+ and HCO^+ , we recommend the use of larger chemical networks and a careful treatment of the ionization (metal abundances, freeze-out, charge exchange and grain charging).

The effects outlined above are all related to differences in the chemical input data. It is widely known that many of the rates we use bear large uncertainties and some reaction pathways may be even debated. In addition, we did not even include surface chemistry here, a new layer of complexity with even more unknown parameters. It becomes clear that interpreting absolute column densities of fluxes from molecular lines will be affected by the specific choice of database and/or size of the network used. This

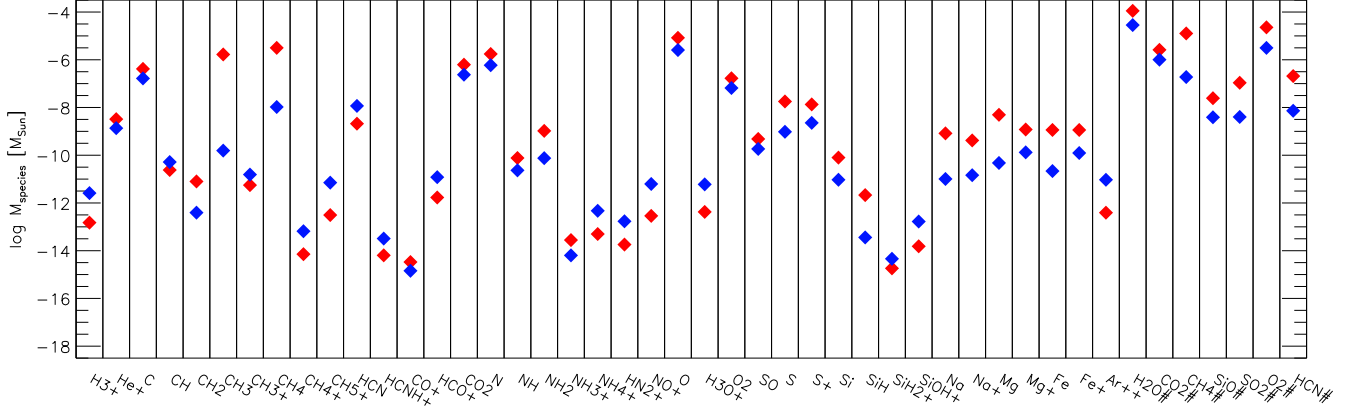


Fig. 16. Differences in species masses using the UMIST2012 database and its adsorption energies for the small (red, model 6) and large chemical network (blue, model 8).

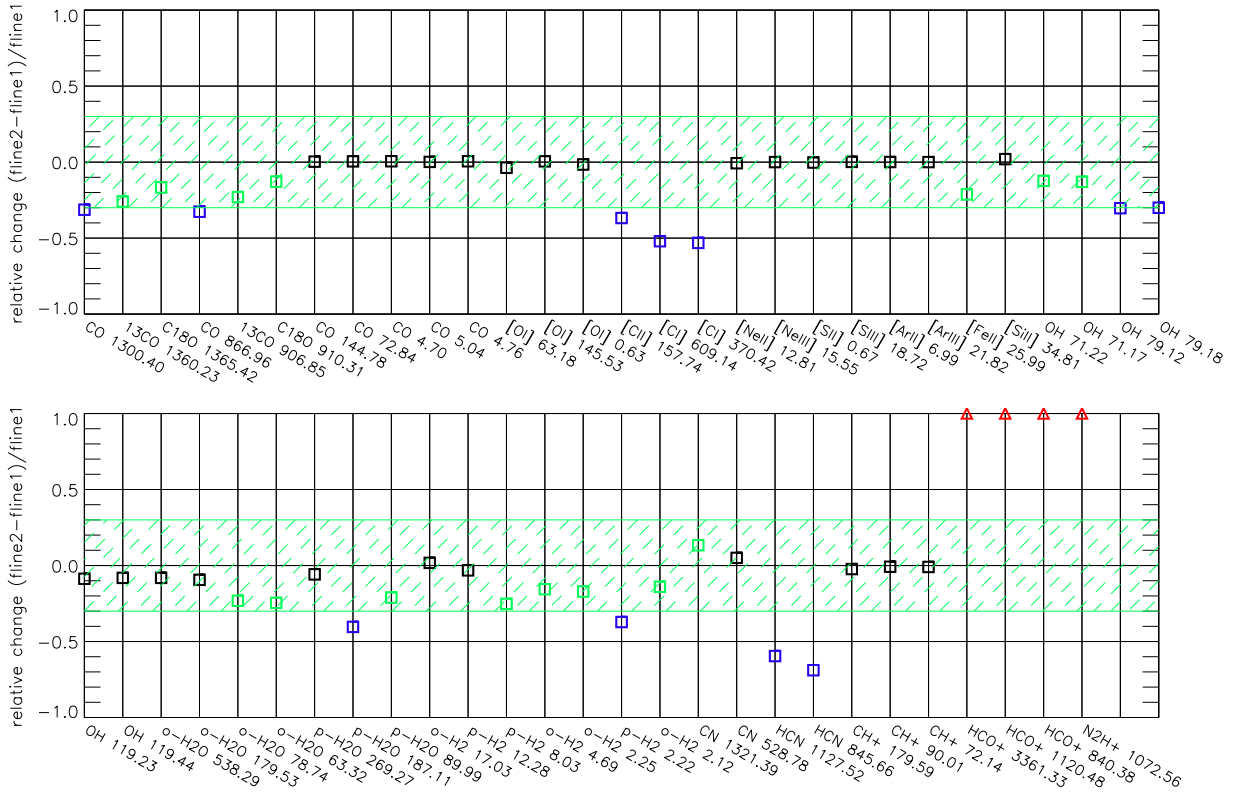


Fig. 17. Comparison of line fluxes using the UMIST2012 database and its adsorption energies for the small (fine1, model 6) and large chemical network (fine2, model 8). Black and green squares denote differences of less than 25% and less than a factor two respectively, blue squares and red triangles denote differences larger than a factor three and ten respectively.

poses especially a problem when comparing works from different groups using different chemical input data. It also puts a limit to the quantitative interpretation of individual line observations. A more robust approach could be a differential investigation of the impact of specific disk parameters on key observables, e.g. the flaring angle, the gas mass, the amount of irradiation. Even though the absolute column densities of specific species may not be known to better than a factor few, the relative changes should be trustworthy.

5. Conclusions

From the detailed investigation of various chemical databases, different sets of adsorption energies and sizes of chemical networks, we conclude the following key points.

Many atomic and molecular lines are very robust against changes in the chemical rates and in the size of the network. Caution, however, is required for

- HCN, N_2H^+ and HCO^+ lines (size of the network),
- high excitation CO, CN, CH^+ , H_2O , OH lines (database dependency),

- CH⁺ lines (reactions of excited H₂),
- HCO⁺ lines (UMIST2006 to UMIST2012 update in rates).

Collider reactions play a major role even in the upper layers of disks. Hence, it would be good to revisit those in experiments. Special attention should be given to checking their low temperature extrapolations.

There is not a single consistent set of adsorption energies to be used for disks. Instead, we recommend a self-consistent approach, where the adsorption energy depends on the nature of the already existing ice, e.g. polar or non-polar. This is of minor importance for most of the observed gas lines. However, it will affect the spatial position of ice lines in the disk and thus the emitting region of the rarer CO isotopologues and molecular ions such as HCO⁺ and N₂H⁺.

For CH⁺ state-to-state reactions become important in the upper layers of disks. Only very few reactions of excited molecular hydrogen have so far been investigated in detail. The here proposed simplified scheme of using the H₂ $\nu = 1$ state and scaling the known reaction rates for H₂ $\nu = 0$ can only be a first step.

As demonstrated here, the absolute line fluxes can be very sensitive to the specific choice of rate network. However, this will not affect studies where the sensitivity of lines is tested against specific disk parameters using the same chemical network and database. However, discrepancies in disk models for specific objects from groups using different chemical networks should be taken with caution.

More recent discussions among the disk modelers and the chemical database groups start to diminish some of the discrepancies noted in this work. Hence, we expect that new database releases will bring the results in even closer agreement.

Acknowledgements. We would like to thank K. Oeberg, E. Bergin, T. Millar and E. van Dishoeck for insightful discussions during the development of this work. We also thank the anonymous referee for a careful reading of the manuscript and suggestions that improved the clarity of the figures and text. IK, WFT, CR, and PW acknowledge funding from the EU FP7- 2011 under Grant Agreement nr. 284405. CR also acknowledges funding by the Austrian Science Fund (FWF), project number P24790.

Appendix A: Chemical reaction rates

Next to the standard rates from chemical databases such as UMIST, OSU or KIDA, we use the additional set of reaction rates described below. Some of them are added to the standard set of rates, some overwrite rates from the databases if this option is invoked. This is indicated in the respective subsections. Abbreviations for the references are listed in Table A.1.

A.1. Chemistry different from UMIST

A key reaction is the H₂ formation which is hardcoded in ProDiMo. The reaction rate and implementation is described in Woitke et al. (2009a).

A.2. Chemistry added to UMIST

Reactions which we include in addition to UMIST are given in Table A.2. Most of them describe the photodissociation of molecular ions; these latter rates are taken from Heays et al. (2017). We use the formalism of (Woitke et al. 2009a) to implement adsorption of gas phase species onto grains and thermal and non-thermal desorption.

Table A.1. List of reference abbreviations

Abbreviation	Reference
A93	Anicich (1993)
A96	Aikawa et al. (1996a)
AG-estimate	Al Glassgold private communication
B06	Badnell (2006)
BC92	Baulch et al. (1992)
EF03	Eiteneer & Frenklach (2003)
FS06	Fontijn et al. (2006)
G01	Girardet & Toubin (2001)
H17	Heays et al. (2017)
HH93	Hasegawa & Herbst (1993)
HM89	Hollenbach & McKee (1989)
HM97	Hierl et al. (1997)
HTT91	Hollenbach et al. (1991)
H09	Hollenbach et al. (2009)
JB86	Jones et al. (1986)
JR99	Jodkowski et al. (1999)
KR97	Kruse & Roth (1997)
KY90	Koshi et al. (1990)
L88	Lennon et al. (1988)
LF91	Landini & Fossi (1991)
MM99	Mebel et al. (1999)
TH85	Tielens & Hollenbach (1985)
TH86	Tsang & Hampson (1986)
T87	Tsang (1987)
vD08	van Dishoeck et al. (2008)
VY95	Verner & Yakovlev (1995)
ZZ98	Zhu et al. (1998)

A.3. Photochemistry

We calculate the photo rates from using the local radiation field from the 2D continuum radiative transfer (Kamp et al. 2010) and the photoionization and -dissociation cross sections from the Leiden database (van Dishoeck et al. 2008; Heays et al. 2017). These rates replace the standard UMIST photo rates even if the UMIST database is chosen.

A.4. Chemistry of excited H₂

Reactions of excited H₂ (H2EXC, H₂^{*}) are neither included in UMIST2006 nor in UMIST2012. They can be important in disks, especially at the surface and thus have been included in Reactions.in. The basic assumption is that the vibrational energy of the excited H₂ can be entirely used to overcome a potential reaction barrier (Tielens & Hollenbach 1985). While this might be a reasonable assumption for low barriers, it may overestimate the rates for reactions with a high barrier. *In any case all those rates should be treated as guesses at most.* In the absence of any better rates, the reaction rate of a species with H₂ is simply modified by subtracting the energy corresponding to the first vibrational excited level $\nu = 1$, 5980 K.

The collisional de-excitation rate (in units of cm³ s⁻¹) of the pseudo excited state (effective quantum number $\nu = 6$) H₂^{*} by collisions with H and H₂ is taken from Tielens & Hollenbach (1985) as one-sixth of the collisional de-excitation rate from $\nu = 1$, $\gamma_{10}^{\text{H,H}_2}$

$$R_{ul}^{\text{H}} = 2.887 \cdot 10^{-12} \left(\frac{T}{300} \right)^{0.5} \exp(-1000/T) \quad (\text{A.1})$$

$$R_{ul}^{\text{H}_2} = 4.042 \cdot 10^{-12} \left(\frac{T}{300} \right)^{0.5} \exp(-18100/(T+1200)) \quad (\text{A.2})$$

Table A.2. Rate constants for reactions added on top of the UMIST database.

reaction	A	B	C	temperature range	reference
$\text{CH}_5^+ + h\nu \rightarrow \text{CH}_4^+ + \text{H}$	3.00(-11)	0.0	2.0	10.0 - 41000.0	H17
$\text{CH}_5^+ + h\nu \rightarrow \text{CH}_3^+ + \text{H}_2$	3.00(-11)	0.0	2.0	10.0 - 41000.0	H17
$\text{H}_2\text{O} + h\nu \rightarrow \text{O} + \text{H}_2$	8.89(-11)	3.90	4.12	10.0 - 41000.0	H17
$\text{H}_2\text{O}^+ + h\nu \rightarrow \text{O} + \text{H}_2^+$	5.00(-13)	0.0	2.0	10.0 - 41000.0	H17
$\text{H}_2\text{O}^+ + h\nu \rightarrow \text{O}^+ + \text{H}_2$	5.00(-13)	0.0	2.0	10.0 - 41000.0	H17
$\text{H}_3\text{O}^+ + h\nu \rightarrow \text{H}_2\text{O} + \text{H}^+$	2.00(-11)	0.0	2.0	10.0 - 41000.0	H17
$\text{H}_3\text{O}^+ + h\nu \rightarrow \text{OH} + \text{H}_2^+$	1.00(-11)	0.0	2.0	10.0 - 41000.0	H17
$\text{H}_3\text{O}^+ + h\nu \rightarrow \text{H}_2\text{O}^+ + \text{H}$	2.00(-11)	0.0	2.0	10.0 - 41000.0	H17
$\text{H}_3\text{O}^+ + h\nu \rightarrow \text{OH}^+ + \text{H}_2$	2.00(-11)	0.0	2.0	10.0 - 41000.0	H17
$\text{SiOH}^+ + h\nu \rightarrow \text{SiO}^+ + \text{H}$	5.00(-11)	0.0	2.0	10.0 - 41000.0	H17
$\text{NH}^+ + h\nu \rightarrow \text{N}^+ + \text{H}$	5.40(-11)	0.0	1.64	10.0 - 41000.0	vD08
$\text{C}^+ + \text{SiO} \rightarrow \text{SiO}^+ + \text{C}$	5.40(-10)	0.0	0.0	10.0 - 41000.0	TH85
$\text{H}_2 + \text{H}_2 \rightarrow \text{H}_2 + \text{H} + \text{H}$	2.30(-11)	1.25	65000.0	10.0 - 41000.0	TH85
$\text{CO} + \text{H} \rightarrow \text{HCO}$	5.29(-34)	0.0	370.0	10.0 - 41000.0	NIST

Notes. The coefficients A , B , and C have their usual meaning (see e.g. McElroy et al. 2013). The notation $x(y)$ denotes $x \cdot 10^y$.

Note that Tielens & Hollenbach (1985) provide in their Table 9 a de-excitation rate for collisions with atomic hydrogen that is a factor 0.67 smaller than this. The collisional excitation rates (in units of $\text{cm}^3 \text{s}^{-1}$) are the inverse of these de-excitation rates (Woitke et al. 2009a) using the energy of the pseudo-level for vibrationally excited H_2 , $E_v = 2.6 \text{ eV}$,

$$R_{lu}^{\text{H}} = R_{ul}^{\text{H}} \exp(-E_v/kT_{\text{gas}}) \quad (\text{A.3})$$

$$R_{lu}^{\text{H}_2} = R_{ul}^{\text{H}_2} \exp(-E_v/kT_{\text{gas}}) \quad (\text{A.4})$$

Other rates are taken explicitly from their Table 9.

Agúndez et al. (2010) use for the reaction $\text{H}_2^* + \text{C}^+ \rightarrow \text{CH}^+ + \text{H}$ a constant Langevin rate coefficient of $1.6 \cdot 10^{-9} \text{ cm}^3 \text{ s}^{-1}$. Fig.10 of Hierl et al. (1997) suggest a possible weak temperature dependence. Zanchet et al. (2013b) performed quantum calculations to derive state-to-state reaction rates for the system C^+ and H_2 . In the following, we neglect the formation excitation of CH^+ and use the parametrized rate from Zanchet et al. (2013a) for $\text{H}_2(\nu = 1)$ (Table 3). To bring it into the usual form, we present here a simple Arrhenius fit

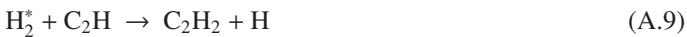
$$R = 3.87 \cdot 10^{-10} \left(\frac{T}{300}\right)^{-0.136} \exp(-4.33/T) \text{ cm}^3 \text{ s}^{-1} \quad (\text{A.5})$$

The theoretical calculations are a factor 4 lower than the laboratory work from Hierl et al. (1997) (Fig. A.1). The newer rate is only used in Sect. 3.5 discussing the effect of excited H_2 on the chemistry.

In addition to those reactions, we add



taken from Zhu et al. (1998) and Jones et al. (1986), respectively. In the latter case, $R = 0.18 - 1.8 \cdot 10^{-9} \text{ cm}^3/\text{s}$ and we approximate that with $0.5 \cdot 10^{-9} \text{ cm}^3/\text{s}$.



taken from NIST (Kruse & Roth 1997; Eiteneer & Frenklach 2003). The activation barriers of 4000 K, 460.6 K (respectively) are set to zero.

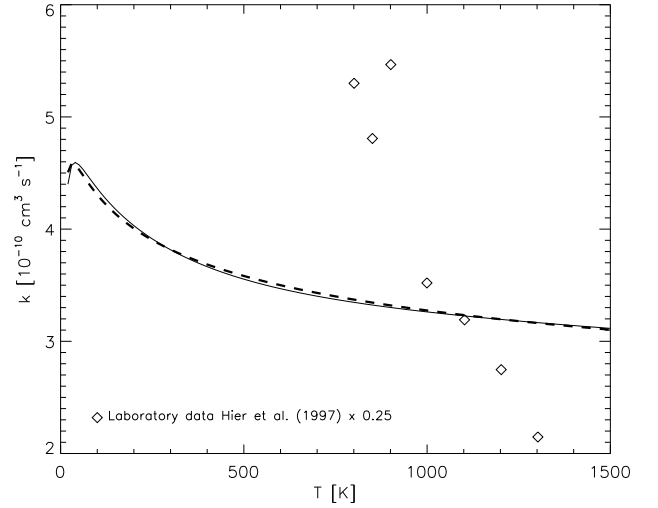


Fig. A.1. Comparison of the theoretically calculated rate A.7 (solid line, Zanchet et al. 2013a), the laboratory data scaled by a factor 0.25 (diamonds, Hierl et al. 1997) and the fit presented here (dashed line).

taken from NIST (Tsang & Hampson 1986; Baulch et al. 1992). The first one has only an upper limit and we use that for the rate and set the activation barrier of 6400 K to 420 K. The activation barrier of 4740 K for the second one is set to zero.



taken from NIST (Jodkowski et al. 1999; Tsang 1987). The activation barriers of 2470 K, 6720 K (respectively) are set to zero and 740 K respectively.



taken from NIST (Koshi et al. 1990; Fontijn et al. 2006; Mebel et al. 1999). The activation barriers of 16600 K, 7760 K, 3610 K (respectively) are set to 12115 K, 1802 K and zero re-

spectively.



are taken from UMIST2006 and their activation barriers of 11700 K and 1943 K are set to 5720 K and zero respectively.



are taken from UMIST2006 and their activation barriers of 3150 K, 1736 K, 21890 K are set to zero, zero and 15910 K respectively.



are taken from UMIST2006 and their activation barriers of 55000 K, 84100 K, 84100 K are set to 49020 K, 78120 K, and 72260 K.

A.5. Collider reactions

Even though UMIST2006 contains collider (three-body reactions, CL), the UMIST2012 rate file does not. There are 32 collider reactions in UMIST2006 (#4552–#4583). After discussion with T. Millar, we decided to append them to the UMIST2012 data file.

A.6. PAH chemistry

PAHs participate in charge exchange reactions with other gas-phase species or the ionised PAHs can recombine with electrons. Therefore PAHs are a key species to the modelling of the gas heating and key to the determination of the ionisation fraction in disks. An example of the role of PAHs is for example that negative PAHs can lock a large fraction of the free electrons, preventing them to recombine with HCO^+ or N_2H^+ , two commonly detected species in protoplanetary disks. The PAH reactions are described in details in Thi et al., (in prep.). PAHs can adsorb onto the surfaces of grains and desorb through photons or thermal heating depending on their sizes. PAH freeze-out can modify the heating-cooling balance as well as the ionisation fraction in disks. The ionisation balance is calculated using the local UV radiation field (Woitke et al. 2011). The models described in this paper use circumcoronene ($\text{C}_{54}\text{H}_{18}$) as the representative PAH. Circumcoronene is a large and compact PAH (pericondensed, superaromatic) and the electron delocalization adds to its stability against photodissociation (Tielens et al. 1987; Visser et al. 2007; De Becker 2013).

A.6.1. PAH freeze-out and desorption

PAHs can adsorb onto grain surfaces coated with water ice or on bare silicate grains. In dense molecular clouds, weak absorption features have been attributed to PAHs frozen in water ice mantles (Bouwman et al. 2011a). Bouwman et al. (2011b) estimated that the $\text{PAH}_{\text{ice}}/\text{H}_2\text{O}_{\text{ice}}$ ratio can reach as much as 2%. Assuming a water ice abundance of $\sim 10^{-5}$, the PAH# (PAHs adsorbed on dust surfaces) abundance is $\sim 2 \times 10^{-7}$, which suggests that all the PAHs are removed from the gas phase (the total

PAH abundance is estimated to be $\sim 3 \times 10^{-7}$). The standard PAH used in the models presented here is circumcoronene although one can choose also larger condensed PAHs such as circumcircumcoronene ($\text{C}_{96}\text{H}_{24}$), which are even more stable against photodissociation than circumcoronene.

In the absence of measured desorption rates for all individual PAHs, we assume a linear dependance of the desorption energy on the number of carbon and hydrogen atoms of the PAH based on the method of fragment constant. The linear behaviour is consistent with the additivity of van der Waals interactions (Björk et al. 2011). Adsorption (desorption) energies E_{ads} measured in the laboratory vary from $E_{\text{ads}}/k \simeq 5600$ K for benzene C_6H_6 (Thrower et al. 2009a) up to $E_{\text{ads}}/k \simeq 18900$ K for pentacene $\text{C}_{22}\text{H}_{14}$ (Oja & Suuberg 1998). Table A.3 summarises the adsorption (desorption) energies for several PAHs. It should be noted that the surface on which the PAHs are adsorbed varies in the different studies. We plotted the adsorption energy normalised by the number of carbon atoms $E_{\text{des}}/N_{\text{C}}$ as a function of $N_{\text{H}}/N_{\text{C}}$ in Fig. A.3. The adopted law is

$$E_{\text{ads}}/k = (482 \times (N_{\text{C}} - N_{\text{H}})) + (946 \times N_{\text{H}}) \text{ K} , \quad (\text{A.25})$$

where N_{C} is the number of carbon atoms of the PAH and N_{H} is the number of hydrogen. E_{CC}/k ($= 482$ K) is the fitted desorption energy per graphene-like carbon, i.e. carbon atoms not attached to hydrogen and E_{CH}/k ($= 946$ K) is the fitted energy per benzene-like carbon and its adjoining H-atom. Graphene-like carbons are C-atoms with three covalent bonds with carbons, whereas benzene-like carbon have two covalent bonds with carbons and one bond with a hydrogen atom. Graphenes are PAHs where all the hydrogens have been stripped away. The value for E_{CC}/k is consistent with the measured range of adsorption energies of graphene on amorphous SiO_2 , which lies between 450 and 1685 K per carbon (Thrower et al. 2013; Kumar et al. 2016). The adsorption energies are also consistent with the theoretical values of Mészár et al. (2013).

The fitting formula is valid for PAH made of up to 100 carbon atoms. For bigger PAHs, the formula gives values that are larger than the heat of vaporization of graphite of $\Delta H_{\text{f}}/k = 86240$ K, Fig. A.4 (Pierson 1993). For circumcoronene, the estimated desorption energy is 34380 K. A simple way to estimate the condensation temperature T_{cond} is to balance the adsorption with the thermal desorption

$$\sigma_{\text{dust}} n_{\text{dust}} n_{\text{PAH}} S_{\text{PAH}} \sqrt{\frac{8kT_{\text{cond}}}{\pi m_{\text{PAH}}}} = n_{\text{PAH}} \nu_{\text{osc}} \exp(-E_{\text{des}}/kT_{\text{cond}}) , \quad (\text{A.26})$$

where the exponential prefactor is (Aikawa et al. 1996b)

$$\nu_{\text{osc}} = \sqrt{\frac{2n_{\text{surf}} E_{\text{des}}}{\pi^2 m_{\text{PAH}}}} \text{ s}^{-1} . \quad (\text{A.27})$$

S_{PAH} is the sticking coefficient for PAH molecules and n_{PAH} and $n_{\text{PAH}\#}$ are the number density of PAH in the gas phase and adsorbed on surfaces respectively. The number of surface adsorption sites is assumed to be $n_{\text{surf}} = 1.5 \times 10^{15} \text{ cm}^{-2}$ for grains with a radius of $0.1 \mu\text{m}$. The average number of dust grains in the disk is

$$n_{\text{d}} = \frac{2.2 \text{ amu } n_{\text{H}}}{(4/3)\pi\rho_{\text{d}} <a^3> \delta} \approx 2.907 \times 10^{-15} n_{\text{H}} \left(\frac{\mu\text{m}^3}{<a^3>} \right) \left(\frac{100}{\delta} \right) , \quad (\text{A.28})$$

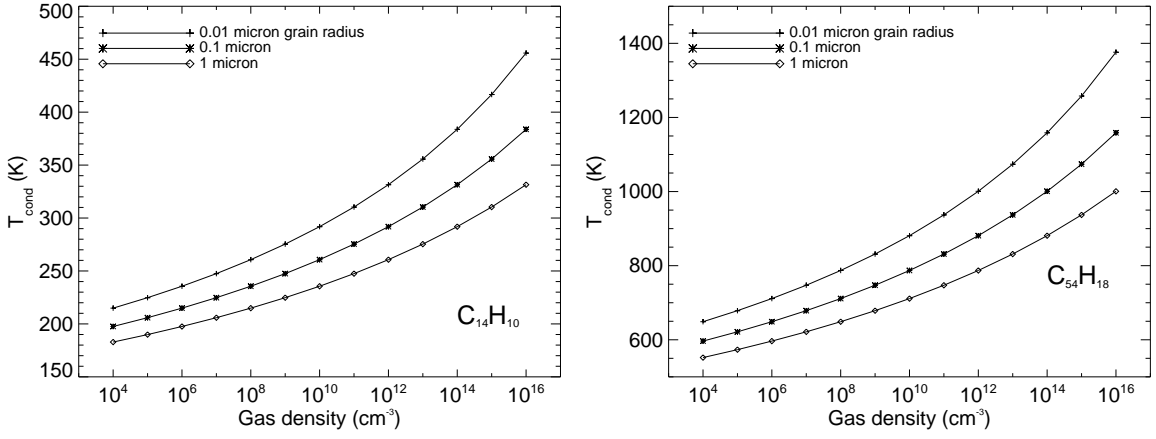


Fig. A.2. PAH condensation temperature for anthracene ($C_{14}H_{10}$) and circumcoronene ($C_{54}H_{18}$) assuming three different grain radii.

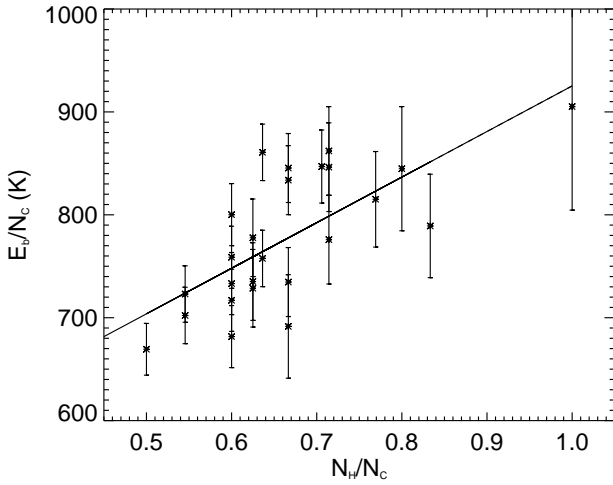


Fig. A.3. PAH binding energy normalized to the number of carbon atoms.

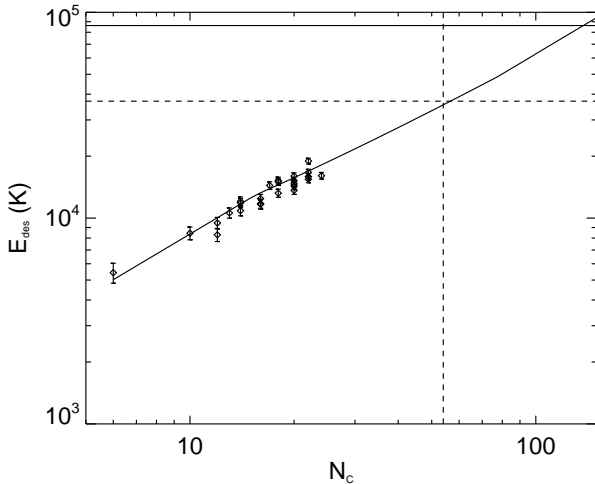


Fig. A.4. PAH desorption energy. The horizontal line corresponds to the limit imposed by the heat of vaporisation of graphite. The dashed-lines designate the desorption energy for circumcorene ($N_C = 54$).

where δ is the gas-to-dust mass ratio which is assumed to be 100. We have assumed a silicate mass density of 3.0 g cm^{-3} .

The balance between adsorption and thermal desorption for a gas density of 10^{10} cm^{-3} , a grain radius of $1 \mu\text{m}$, a gas-to-dust mass ratio of 100, and assuming $n_{\text{PAH}} = n_{\text{PAH}\#}$ and a sticking coefficient of unity, leads to a condensation temperature for circumcoronene of $\sim 710 \text{ K}$. In disks, PAHs should stick onto silicate grains and to each other. The condensation temperature for anthracene and circumcoronene is shown in Fig. A.2. The desorption of PAHs occurs thermally, induced by cosmic ray hits on the grains, and by absorption of a UV photon. We assumed a yield of 10^{-3} per absorbed photon for the photodesorption and a standard cosmic-ray induced desorption similar to the other ice species. The encounter between two PAHs can also result in the formation of clusters, which may subsequently grow by further accretion of PAHs. However, this mechanism is not accounted for in our current model.

A.7. X-ray chemistry

The X-ray chemistry in ProDiMo is described in detail in the appendix of Meijerink et al. (2012). Abbreviations for the references are listed in Table A.1.

The individual atomic ionization cross sections are used to derive the molecular dissociation rate from the individual ionization rates using the relative weight difference. If the difference in atomic weight between the components of the molecule is large, the cross section of the heavier one is used. If the difference is small, the cross sections are combined (Aresu et al. 2011). An example is the reaction $\text{CO} + \text{XPHOT}$ which can lead to $\text{C}^{2+} + \text{O}$, $\text{C}^+ + \text{O}^+$, or $\text{C} + \text{O}^{2+}$, so that the total cross section is the sum

$$\sigma_{\text{CO}} = \frac{1}{3}\sigma_{\text{C}} + \frac{1}{6}(\sigma_{\text{C}} + \sigma_{\text{O}}) + \frac{1}{3}\sigma_{\text{O}} \quad (\text{A.29})$$

where σ_{El} is the ionization cross sections of the element, in this case C and O.

More detailed explanations/discussions of rates can be found in Ádámkóvics et al. (2011). The di-electronic recombination rates are from tables of Landini & Fossi (1991), Badnell et al. (2003), Badnell (2006), Zatsarinny et al. (2003) and subsequent papers of this series. In case of X-rays, the high temperature di-electronic recombination rates get added to the radiative recombination rates taken from UMIST. The two elements Ne and Ar have only di-electronic recombination rates currently available. We include here also charge exchange reaction of Ar and Ne with water, O_2 , CO , N_2 , CH_4 , NH_3 , CO_2 , and NO . In addition we consider charge exchange between He^+ and Ne.

Table A.3. Measured and computed (Mészár) PAH desorption energies.

Name	Formula	Oja98	Thower09	Domine07	Fu11	Goldfarb08	Meszar13	Thower13
		E_{des} [K]						
benzene	C ₆ H ₆		5431					
naphtalene	C ₁₀ H ₈						8448	
acenaphthylene	C ₁₂ H ₈					8298 ± 989		
acenaphthene	C ₁₂ H ₁₀					9470 ± 269		
fluorene	C ₁₃ H ₁₀					1059 ± 229		
anthracene	C ₁₄ H ₁₀	12068				11848 ± 399		
phenanthrene	C ₁₄ H ₁₀	10860		10862				
fluoranthene	C ₁₆ H ₁₀					11658 ± 332		
pyrene	C ₁₆ H ₁₀	12442				11762 ± 392		
2,3-benzofluorene	C ₁₇ H ₁₂	14397						
naphthacene	C ₁₈ H ₁₂	15218				15006 ± 350		
perylene	C ₂₀ H ₁₂	16003				15175 ± 98		
benzo[a]phenanthrene	C ₁₈ H ₁₂					13224 ± 430		
benzo[a]pyrene	C ₂₀ H ₁₂					13633 ± 375		
benzo[b]fluoranthene	C ₂₀ H ₁₂				14337			
benzo[k]fluoranthene	C ₂₀ H ₁₂				14663			
benzo[ghi]perylene	C ₂₂ H ₁₂				15448			
indeno[1,2,3-cd]pyrene	C ₂₂ H ₁₂				15906			
dibenz[a,h]anthracene	C ₂₂ H ₁₄				16667			
pentacene	C ₂₂ H ₁₄	18936						
coronene	C ₂₄ H ₁₂	16063						19727

Notes. Oja98: Oja & Suuberg (1998); Thower09: Thower et al. (2009b); Domine07: Domine et al. (2007); Fu11: Fu & Suuberg (2011); Goldfarb08: Goldfarb & Suuberg (2008); Meszar13: Mészár et al. (2013); Thower13: Thower et al. (2013)

Appendix B: How E_{ads} affects line fluxes

We show in Figs. B.1 to B.3 how models with different sets of adsorption energies (Aikawa, GH06, UMIST2012 and temperature-dependent E_{ads}) affect our selection of line fluxes.

References

- Ádámkóvics, M., Glassgold, A. E., & Meijerink, R. 2011, *ApJ*, 736, 143
 Agúndez, M., Cernicharo, J., & Goicoechea, J. R. 2008, *A&A*, 483, 831
 Agúndez, M., Goicoechea, J. R., Cernicharo, J., Faure, A., & Roueff, E. 2010, *ApJ*, 713, 662
 Aikawa, Y. & Herbst, E. 2001, *A&A*, 371, 1107
 Aikawa, Y., Miyama, S. M., Nakano, T., & Umebayashi, T. 1996a, *ApJ*, 467, 684
 Aikawa, Y., Miyama, S. M., Nakano, T., & Umebayashi, T. 1996b, *ApJ*, 467, 684
 Anicich, V. G. 1993, *J. Phys. Chem. Ref. Data*, 22, 1469
 Antonellini, S. 2016, PhD thesis, Kapteyn Astronomical Institute, University of Groningen, Landleven 12, 9700 AV Groningen, The Netherlands
 Antonellini, S., Kamp, I., Riviere-Marichalar, P., et al. 2015, *A&A*, 582, A105
 Aresu, G., Kamp, I., Meijerink, R., et al. 2011, *A&A*, 526, A163
 Aresu, G., Meijerink, R., Kamp, I., et al. 2012, *A&A*, 547, A69
 Avramenko, L. I. & Krasnenkov, V. M. 1966, *Bull. Acad. Sci. USSR Div. Chem. Sci. (Engl. Transl.)*, 15, 394
 Badnell, N. R. 2006, *ApJS*, 167, 334
 Badnell, N. R., O’Mullane, M. G., Summers, H. P., et al. 2003, *A&A*, 406, 1151
 Baulch, D. L., Cobos, C. J., Cox, R. A., et al. 1992, *J. Phys. Chem. Ref. Data*, 21, 411
 Bergin, E. A. & Langer, W. D. 1997, *ApJ*, 486, 316
 Bergin, E. A., Langer, W. D., & Goldsmith, P. F. 1995, *ApJ*, 441, 222
 Bethell, T. J. & Bergin, E. A. 2011, *ApJ*, 739, 78
 Björk, J., Stafström, S., & Hanke, F. 2011, *Journal of the American Chemical Society*, 133, 14884
 Bouwman, J., Cuppen, H. M., Steglich, M., Allamandola, L. J., & Linnartz, H. 2011a, *A&A*, 529, A46
 Bouwman, J., Mattioda, A. L., Linnartz, H., & Allamandola, L. J. 2011b, *A&A*, 525, A93
 Ceccarelli, C. & Dominik, C. 2005, *A&A*, 440, 583
 Ceccarelli, C., Dominik, C., Caux, E., Lefloch, B., & Caselli, P. 2005, *ApJ*, 631, L81
 Cernicharo, J., Ceccarelli, C., Ménard, F., Pinte, C., & Fuente, A. 2009, *ApJ*, 703, L123
 Collings, M. P., Anderson, M. A., Chen, R., et al. 2004, *MNRAS*, 354, 1133
 Cuppen, H. M., Walsh, C., Lamberts, T., et al. 2017, *Space Sci. Rev.*
 De Becker, M. 2013, *Bulletin de la Societe Royale des Sciences de Liege*, 82, 33
 Dere, K. P., Landi, E., Mason, H. E., Monsignori Fossi, B. C., & Young, P. R. 1997, *A&AS*, 125, 149
 Domine, F., Cincinelli, A., Bonnaud, E., Martellini, T., & Picaud, S. 2007, *Environmental Science & Technology*, 41, 6033
 Dutrey, A., Henning, T., Guilloteau, S., et al. 2007, *A&A*, 464, 615
 Eiteneer, B. & Frenklach, M. 2003, *Int. J. Chem. Kinet.*, 35, 391
 Fedele, D., Bruderer, S., van Dishoeck, E. F., et al. 2013, *A&A*, 559, A77
 Fontijn, A., Shamsuddin, S. M., Crammond, D., Marshall, P., & Anderson, W. R. 2006, *Combust. Flame*, 145, 543
 Fu, J. & Suuberg, E. M. 2011, *The Journal of Chemical Thermodynamics*, 43, 1660
 Garrod, R. T. & Herbst, E. 2006, *A&A*, 457, 927
 Girardet, C. & Toubin, C. 2001, *Surface Science Reports*, 44, 159
 Glassgold, A. E., Meijerink, R., & Najita, J. R. 2009, *ApJ*, 701, 142
 Goldfarb, J. L. & Suuberg, E. M. 2008, *Journal of Chemical & Engineering Data*, 53, 670
 Harada, N., Herbst, E., & Wakelam, V. 2010, *ApJ*, 721, 1570
 Hasegawa, T. I. & Herbst, E. 1993, *MNRAS*, 261, 83
 Heays, A. N., Bosman, A. D., & van Dishoeck, E. F. 2017, *A&A*, 602, A105
 Hierl, P. M., Morris, R. A., & Viggiano, A. A. 1997, *J. Chem. Phys.*, 106, 10145
 Hily-Blant, P., Bonal, L., Faure, A., & Quirico, E. 2013, *Icarus*, 223, 582
 Hollenbach, D., Kaufman, M. J., Bergin, E. A., & Melnick, G. J. 2009, *ApJ*, 690, 1497
 Hollenbach, D. & McKee, C. F. 1989, *ApJ*, 342, 306
 Hollenbach, D. J., Takahashi, T., & Tielens, A. G. G. M. 1991, *ApJ*, 377, 192
 Jodkowski, J. T., Rayez, M.-T., & Rayez, J.-C. 1999, *J. Phys. Chem. A*, 103, 3750
 Jones, M. E., Barlow, S. E., Ellison, G. B., & Ferguson, E. E. 1986, *Chem. Phys. Letters*, 130, 218
 Kamp, I., Thi, W.-F., Meeus, G., et al. 2013, *A&A*, 559, A24
 Kamp, I., Tilling, I., Woitke, P., Thi, W., & Hogerheijde, M. 2010, *A&A*, 510, A260000+
 Koshi, M., Yoshimura, M., Fukuda, K., & Matsui, H. 1990, *J. Chem. Phys.*, 93, 8703
 Kruse, T. & Roth, P. 1997, *J. Phys. Chem. A*, 101, 2138
 Kumar, S., Parks, D., & Kamrin, K. 2016, *ACS Nano*, 10, 6552, pMID: 27347793
 Landini, M. & Fossi, B. C. M. 1991, *A&AS*, 91, 183
 Lee, H.-H., Roueff, E., Pineau des Forets, G., et al. 1998, *A&A*, 334, 1047

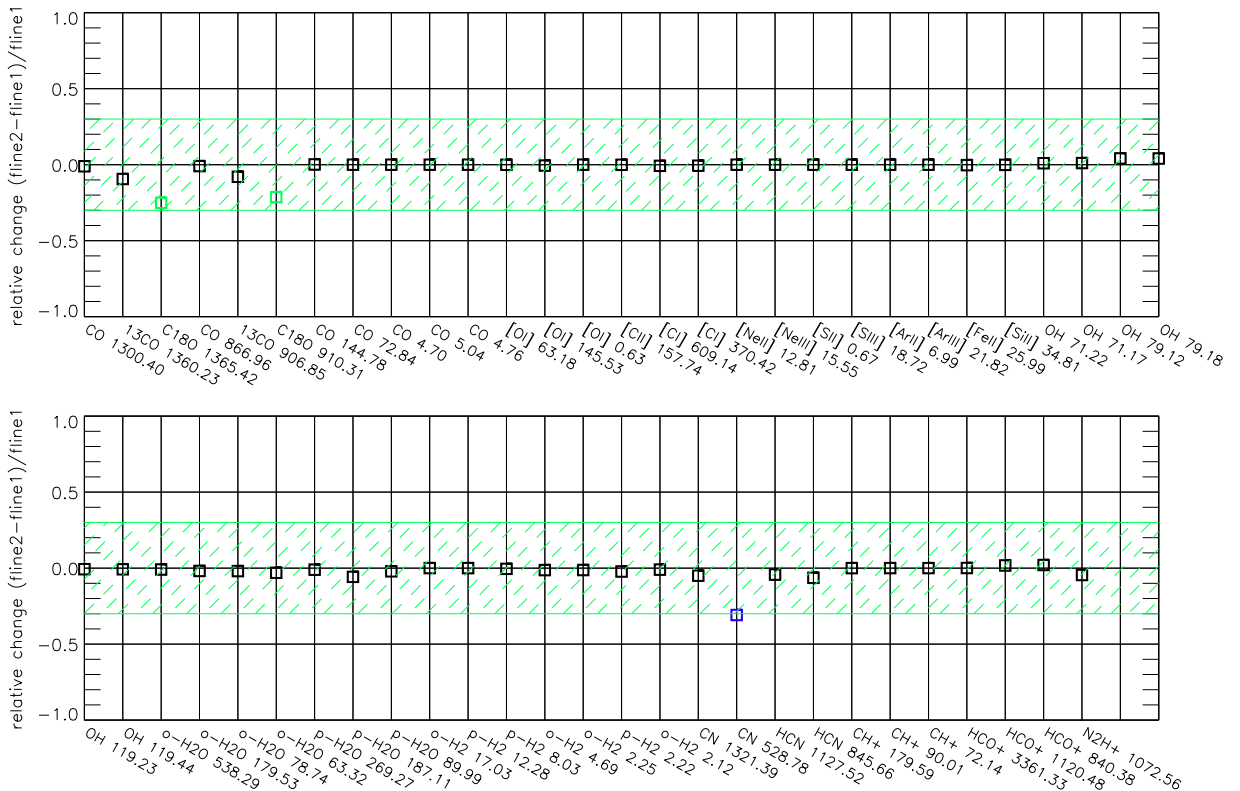


Fig. B.1. Comparison of line fluxes for two sets of adsorption energies: Aikawa (fine1, model 1) and GH06 (fine2, model 5). Black and green squares denote differences of less than 25% and less than a factor two respectively, blue squares and red triangles denote differences larger than a factor three and ten respectively.

- Lennon, M. A., Bell, K. L., Gilbody, H. B., et al. 1988, *J. Phys. Chem. Ref. Data*, 17, 1285
- McElroy, D., Walsh, C., Markwick, A. J., et al. 2013, *A&A*, 550, A36
- Mebel, A., Moskaleva, L. V., & Lin, M. C. 1999, *J. Mol. Struct. THEOCHEM.*, 461, 223
- Meijerink, R., Aresu, G., Kamp, I., et al. 2012, *A&A*, 547, A68
- Mészár, Z. E., Hantal, G., Picaud, S., & Jedlovsky, P. 2013, *The Journal of Physical Chemistry C*, 117, 6719
- Min, M., Bouwman, J., Dominik, C., et al. 2016a, *A&A*, 593, A11
- Min, M., Rab, C., Woitke, P., Dominik, C., & Ménard, F. 2016b, *A&A*, 585, A13
- Nomura, H. & Millar, T. J. 2005, *A&A*, 438, 923
- Öberg, K. I., Qi, C., Fogel, J. K. J., et al. 2010, *ApJ*, 720, 480
- Oja, V. & Suuberg, E. M. 1998, *Journal of Chemical & Engineering Data*, 43, 486
- Panić, O. & Hogerheijde, M. R. 2009, *A&A*, 508, 707
- Pierson, H. O. 1993, *Handbook of carbon, graphite, diamond and fullerenes* (Noyes, New Jersey)
- Prasad, S. S. & Huntress, Jr., W. T. 1980, *ApJS*, 43, 1
- Qi, C., Kessler, J. E., Koerner, D. W., Sargent, A. I., & Blake, G. A. 2003, *ApJ*, 597, 986
- Qi, C., Öberg, K. I., & Wilner, D. J. 2013a, *ApJ*, 765, 34
- Qi, C., Öberg, K. I., Wilner, D. J., et al. 2013b, *Science*, 341, 630
- Rab, C., Elbakyan, V., Vorobyov, E., et al. 2017, *ArXiv e-prints*
- Sandford, S. A. & Allamandola, L. J. 1993, *ApJ*, 417, 815
- Schöier, F. L., van der Tak, F. F. S., van Dishoeck, E. F., & Black, J. H. 2005, *A&A*, 432, 369
- Semenov, D., Wiebe, D., & Henning, T. 2004, *A&A*, 417, 93
- Sternberg, A. & Dalgarno, A. 1995, *ApJS*, 99, 565
- Thi, W.-F., Kamp, I., Woitke, P., et al. 2013, *A&A*, 551, A49
- Thi, W.-F., Ménard, F., Meeus, G., et al. 2011a, *A&A*, 530, L2
- Thi, W.-F., van Zadelhoff, G.-J., & van Dishoeck, E. F. 2004, *A&A*, 425, 955
- Thi, W.-F., Woitke, P., & Kamp, I. 2011b, *MNRAS*, 412, 711
- Throner, J. D., Collings, M. P., Rutten, F. J. M., & McCoustra, M. R. S. 2009a, *MNRAS*, 394, 1510
- Throner, J. D., Collings, M. P., Rutten, F. J. M., & McCoustra, M. R. S. 2009b, *J. Chem. Phys.*, 131, 244711
- Throner, J. D., Friis, E. E., Skov, A. L., et al. 2013, *The Journal of Physical Chemistry C*, 117, 13520
- Tielens, A. G. G. M., Allamandola, L. J., Barker, J. R., & Cohen, M. 1987, in *NATO Advanced Science Institutes (ASI) Series C*, Vol. 191, NATO Advanced Science Institutes (ASI) Series C, ed. A. Leger, L. D'Hendecourt, & N. Boccarda, 273–285
- Tielens, A. G. G. M. & Hollenbach, D. 1985, *ApJ*, 291, 722
- Tsang, W. 1987, *J. Phys. Chem. Ref. Data*, 16
- Tsang, W. & Hampson, R. F. 1986, *J. Phys. Chem. Ref. Data*, 15
- van Dishoeck, E. F. 1990, in *Astronomical Society of the Pacific Conference Series*, Vol. 12, *The Evolution of the Interstellar Medium*, ed. L. Blitz, 207–228
- van Dishoeck, E. F., Jonkheid, B., & van Hemert, M. C. 2008, *ArXiv e-prints*
- Vasyunin, A. I., Semenov, D., Henning, T., et al. 2008, *ApJ*, 672, 629
- Vasyunin, A. I., Sobolev, A. M., Wiebe, D. S., & Semenov, D. A. 2004, *Astronomy Letters*, 30, 566
- Verner, D. A. & Yakovlev, D. G. 1995, *A&AS*, 109, 125
- Visser, R., Geers, V. C., Dullemond, C. P., et al. 2007, *A&A*, 466, 229
- Wakelam, V., Herbst, E., Loison, J.-C., et al. 2012, *ApJS*, 199, 21
- Woitke, P., Kamp, I., & Thi, W.-F. 2009a, *A&A*, 501, 383
- Woitke, P., Min, M., Pinte, C., et al. 2016, *A&A*, 586, A103
- Woitke, P., Riaz, B., Duchêne, G., et al. 2011, *A&A*, 534, A44
- Woitke, P., Thi, W.-F., Kamp, I., & Hogerheijde, M. R. 2009b, *A&A*, 501, L5
- Woodall, J., Agúndez, M., Markwick-Kemper, A. J., & Millar, T. J. 2007, *A&A*, 466, 1197
- Zanchet, A., Agúndez, M., Herrero, V. J., Aguado, A., & Roncero, O. 2013a, *AJ*, 146, 125
- Zanchet, A., Godard, B., Bulut, N., et al. 2013b, *ApJ*, 766, 80
- Zatsarinny, O., Gorczyca, T. W., Korista, K. T., Badnell, N. R., & Savin, D. W. 2003, *A&A*, 412, 587
- Zhu, W., Zhang, J. Z. H., Zhang, Y. C., Zhang, Y. B., & Zhan, L. X. 1998, *J. Chem. Phys.*, 108, 3509

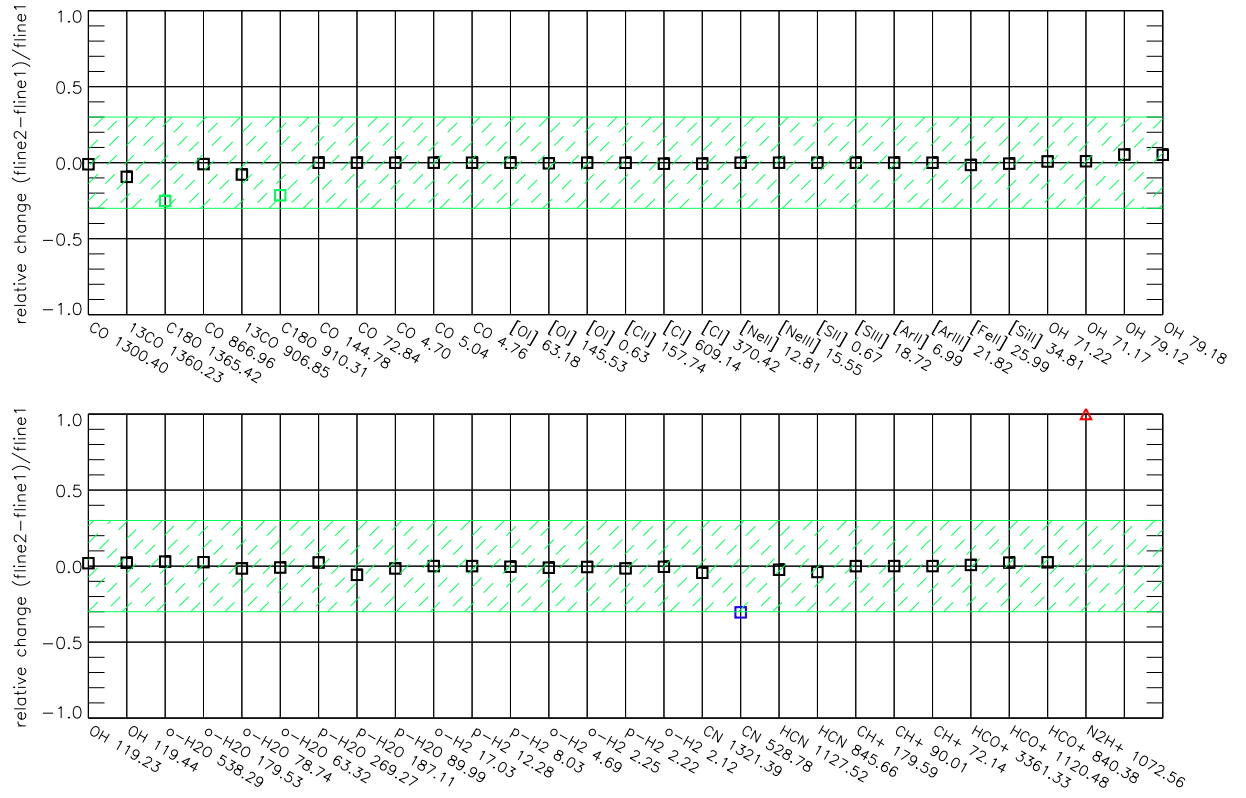


Fig. B.2. Comparison of line fluxes for two sets of adsorption energies: Aikawa (fline1, model 1) and UMIST2012 (fline2, model 6). Black and green squares denote differences of less than 25% and less than a factor two respectively, blue squares and red triangles denote differences larger than a factor three and ten respectively.

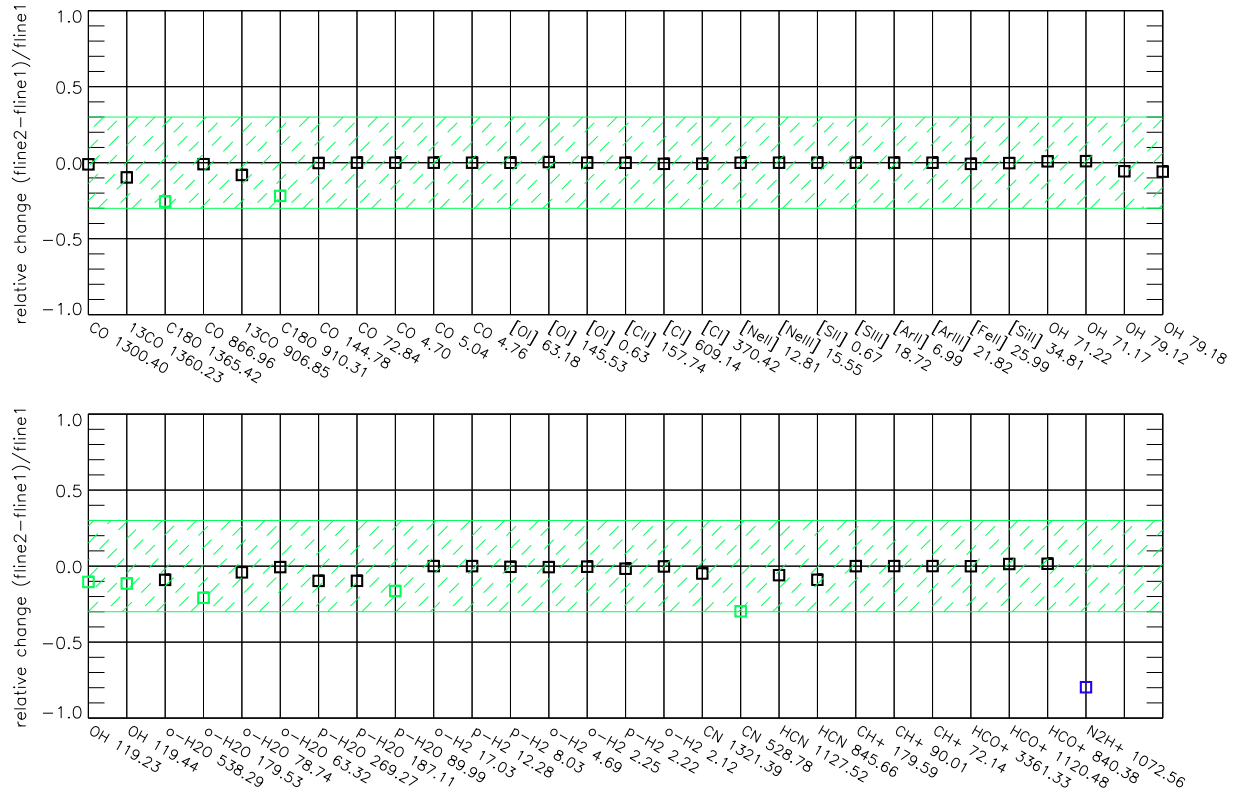


Fig. B.3. Comparison of line fluxes for two sets of adsorption energies: Aikawa (fline1, model 1) and T -dependent adsorption energies (fline2, model 7). Black and green squares denote differences of less than 25% and less than a factor two respectively, blue squares and red triangles denote differences larger than a factor three and ten respectively.